



(PECASE) LIGHT MATTER INTERACTION ON THE NANOSCALE

Xiaoqin Li
UNIVERSITY OF TEXAS AT AUSTIN

01/05/2016
Final Report

DISTRIBUTION A: Distribution approved for public release.

Air Force Research Laboratory
AF Office Of Scientific Research (AFOSR)/ RTA1
Arlington, Virginia 22203
Air Force Materiel Command

REPORT DOCUMENTATION PAGE					Form Approved OMB No. 0704-0188	
<p>The public reporting burden for this collection of information is estimated to average 1 hour per response, including the time for reviewing instructions, searching existing data sources, gathering and maintaining the data needed, and completing and reviewing the collection of information. Send comments regarding this burden estimate or any other aspect of this collection of information, including suggestions for reducing the burden, to the Department of Defense, Executive Service Directorate (0704-0188). Respondents should be aware that notwithstanding any other provision of law, no person shall be subject to any penalty for failing to comply with a collection of information if it does not display a currently valid OMB control number.</p> <p>PLEASE DO NOT RETURN YOUR FORM TO THE ABOVE ORGANIZATION.</p>						
1. REPORT DATE (DD-MM-YYYY) 12/20/2015		2. REPORT TYPE Final Report			3. DATES COVERED (From - To) 10/01/2009-09/30/2015	
4. TITLE AND SUBTITLE Light-Matter Interaction on the Nanoscale				5a. CONTRACT NUMBER		
				5b. GRANT NUMBER FA9550-10-1-0022		
				5c. PROGRAM ELEMENT NUMBER		
6. AUTHOR(S) Xiaoqin LI, Associate Professor of Physics, University of Texas-Austin				5d. PROJECT NUMBER		
				5e. TASK NUMBER		
				5f. WORK UNIT NUMBER		
7. PERFORMING ORGANIZATION NAME(S) AND ADDRESS(ES) Physics Department University of Texas-Austin 2515 Speedway, Austin, TX, 78712					8. PERFORMING ORGANIZATION REPORT NUMBER	
9. SPONSORING/MONITORING AGENCY NAME(S) AND ADDRESS(ES) AFOSR 875 N RANDOLPH ST ARLINGTON VA 22203					10. SPONSOR/MONITOR'S ACRONYM(S)	
					11. SPONSOR/MONITOR'S REPORT NUMBER(S)	
12. DISTRIBUTION/AVAILABILITY STATEMENT approved for public release						
13. SUPPLEMENTARY NOTES program manager at AFOSR is GERNOT POMRENKE						
14. ABSTRACT Studies of light-matter interactions in quantum-confined systems and nanostructures have provided great insight into diverse and fundamental problems such as many-body interactions and entanglement. In particular, optical spectroscopy has proved to be a powerful tool for elucidating electronic dynamics owing to its ability to access information that is difficult or impossible to obtain otherwise. In the initial proposal, we outlined two specific projects: (i) investigation of coherent electronic coupling in semiconductor quantum dot clusters; (ii) investigation of spin wave dynamics in ferromagnetic multilayer structures. In the course of the project, we have expanded the first direction to include investigation of metallic nanoparticles and clusters as well as hybrid nanostructures consisted of both metallic and semiconductor components. In addition, we have studied an emerging class of atomically thin semiconductors known as the transition metal dichalcogenides. In this report, we summarize the key progress occurred during the past 6 years.						
15. SUBJECT TERMS						
16. SECURITY CLASSIFICATION OF:			17. LIMITATION OF ABSTRACT	18. NUMBER OF PAGES	19a. NAME OF RESPONSIBLE PERSON Xiaoqin Li	
a. REPORT	b. ABSTRACT	c. THIS PAGE			19b. TELEPHONE NUMBER (Include area code) 512-471-2063	

INSTRUCTIONS FOR COMPLETING SF 298

1. REPORT DATE. Full publication date, including day, month, if available. Must cite at least the year and be Year 2000 compliant, e.g. 30-06-1998; xx-06-1998; xx-xx-1998.

2. REPORT TYPE. State the type of report, such as final, technical, interim, memorandum, master's thesis, progress, quarterly, research, special, group study, etc.

3. DATES COVERED. Indicate the time during which the work was performed and the report was written, e.g., Jun 1997 - Jun 1998; 1-10 Jun 1996; May - Nov 1998; Nov 1998.

4. TITLE. Enter title and subtitle with volume number and part number, if applicable. On classified documents, enter the title classification in parentheses.

5a. CONTRACT NUMBER. Enter all contract numbers as they appear in the report, e.g. F33615-86-C-5169.

5b. GRANT NUMBER. Enter all grant numbers as they appear in the report, e.g. AFOSR-82-1234.

5c. PROGRAM ELEMENT NUMBER. Enter all program element numbers as they appear in the report, e.g. 61101A.

5d. PROJECT NUMBER. Enter all project numbers as they appear in the report, e.g. 1F665702D1257; ILIR.

5e. TASK NUMBER. Enter all task numbers as they appear in the report, e.g. 05; RF0330201; T4112.

5f. WORK UNIT NUMBER. Enter all work unit numbers as they appear in the report, e.g. 001; AFAPL30480105.

6. AUTHOR(S). Enter name(s) of person(s) responsible for writing the report, performing the research, or credited with the content of the report. The form of entry is the last name, first name, middle initial, and additional qualifiers separated by commas, e.g. Smith, Richard, J, Jr.

7. PERFORMING ORGANIZATION NAME(S) AND ADDRESS(ES). Self-explanatory.

8. PERFORMING ORGANIZATION REPORT NUMBER. Enter all unique alphanumeric report numbers assigned by the performing organization, e.g. BRL-1234; AFWL-TR-85-4017-Vol-21-PT-2.

9. SPONSORING/MONITORING AGENCY NAME(S) AND ADDRESS(ES). Enter the name and address of the organization(s) financially responsible for and monitoring the work.

10. SPONSOR/MONITOR'S ACRONYM(S). Enter, if available, e.g. BRL, ARDEC, NADC.

11. SPONSOR/MONITOR'S REPORT NUMBER(S). Enter report number as assigned by the sponsoring/monitoring agency, if available, e.g. BRL-TR-829; -215.

12. DISTRIBUTION/AVAILABILITY STATEMENT. Use agency-mandated availability statements to indicate the public availability or distribution limitations of the report. If additional limitations/ restrictions or special markings are indicated, follow agency authorization procedures, e.g. RD/FRD, PROPIN, ITAR, etc. Include copyright information.

13. SUPPLEMENTARY NOTES. Enter information not included elsewhere such as: prepared in cooperation with; translation of; report supersedes; old edition number, etc.

14. ABSTRACT. A brief (approximately 200 words) factual summary of the most significant information.

15. SUBJECT TERMS. Key words or phrases identifying major concepts in the report.

16. SECURITY CLASSIFICATION. Enter security classification in accordance with security classification regulations, e.g. U, C, S, etc. If this form contains classified information, stamp classification level on the top and bottom of this page.

17. LIMITATION OF ABSTRACT. This block must be completed to assign a distribution limitation to the abstract. Enter UU (Unclassified Unlimited) or SAR (Same as Report). An entry in this block is necessary if the abstract is to be limited.

Final Report for AFOSR grant FA9550-10-1-0022

Light-Matter Interaction on the Nanoscale

Grant period 10/01/2009-9/30/2016

PI: Xiaoqin (Elaine) Li

Physics department, the University of Texas-Austin, Austin, TX, 78712.

Tel: 512-471-2063; Fax: 512-471-1005; Email: elaineli@physics.utexas.edu

Scientific Progress Report:

Using the support from AFOSR under the PECASE award, the PI has established a world-class optical spectroscopy laboratory and made major advances in several areas of nanophotonics, new atomically thin semiconductors, and spintronics. The flexibility of this program allows the PI to adjust to the most exciting development in these exciting fields in basic science and technology, yet relevant to DoD missions and future operations. We have published 20 articles in peer review journals. It would not be possible to discuss all these accomplishment in this final report. The PI has chosen a few representative works and discussed them in detail.

A. Published Journal Articles

1. Daniel R. Birt, Brian O’Gorman, Maxim Tsoi, **Xiaoqin Li**, Vladislav E. Demidov, and Sergej O. Demokritov, “ Diffraction of spin waves from a submicrometer-size defect in a microwaveguide”, Appl. Phys. Lett. 95, 122510, 2009.
2. Vladislav E. Demidov, and Sergej O. Demokritov, Daniel R. Birt, Brian O’Gorman, Maxim Tsoi, and **Xiaoqin Li**, “ Radiation of spin waves from the open end of a microscopic magnetic-film waveguide”, Phys. Rev. B., 80, 014429, 2009.
3. Meg Creasey, **Xiaoqin Li**, J. H. Lee, Zh. M. Wang, G. J. Salamo, “Strongly Confined Excitons in Self-Assembled InGaAs Quantum Dot Clusters Produced by a Hybrid Growth Method”, J. Appl. Phys., 107, 104302, 2010.
4. Xuhuai Zhang, Marcelo Davanco, Kara Maller, Thomas Jarvis, Chihhui Wu, Dmitriy Korobkin, Yaroslav Urzhumov, **Xiaoqin Li**, Gennady Shvets, Stephen R. Forrest, “Interferometric characterization of a sub-wavelength near-infrared negative index metamaterial”, Opt. Exp.18, 17788, 2010

5. Suenne Kim, Farbod Shafiei, Daniel Ratchford, **Xiaoqin Li**, “Controlled AFM manipulation of small nanoparticles and assembly of hybrid nanostructures”, *Nanotechnology*, 22, 115301, 2011.
6. Daniel Ratchford, Farbod Shafiei, Suenne Kim, Stephen, Gray, **Xiaoqin Li**, “Manipulating Coupling between a single semiconductor quantum dot and single gold nanoparticle”, *Nano Letters*, 11, 1049, 2011.
7. Daniel Ratchford, Konrad Dziatkowski, Thomas Hartsfield, **Xiaoqin Li**, Yan Gao, Zhiyong Tang, “Photoluminescence dynamics of ensemble and individual CdSe/ZnS quantum dots with an alloyed core/shell interface”, *Journal of Applied Physics*, 109, 103509, 2011.
8. Daniel Ratchford, Farbod Shafiei, Stephen Gray, **Xiaoqin Li**, “Polarization properties of a CdSe/ZnS and Au Nanoparticle Dimer”, *ChemPhysChem*, 13, 2522, 2012.
9. Daniel R. Birt, Kyongmo An, Shingo Tamaru, David Ricketts, Kin Wong, Kang Wang, Maxim Tsoi, **Xiaoqin Li** “Deviation from Exponential Decay for Spin Waves Excited with an Coplanar Waveguide Antenna”, *Appl. Phys. Lett.* 101, 252409, 2012
10. Daniel R. Birt, Kyongmo An, Annie Weathers, Li Shi, Maxim Tsoi, **Xiaoqin Li**, “Brillouin Light Scattering Spectra as local Temperature Sensors for Thermal Magnons and Acoustic Phonons” , *Appl. Phys. Lett.* 102, 082401, 2013
11. Megan Creasey, **Xiaoqin Li**, J. H. Lee, Zh. M. Wang, G. J. Salamo, “Self-Assembled InGaAs/GaAs quantum dot molecules with controlled spatial and spectral properties” *Nano Letters*, 12, 5169, 2012.
12. Farbod Shafiei, Chihhui Wu, Patrick Putzke, Yanwen Wu, Akshay Singh, **Xiaoqin Li**, Gennady Shvets “Plasmonic Nano-Protractor Based on Polarization Spectro-Tomography”, *Nature-Photonics*, 7, 367, 2013
13. Farbod Shafiei, Francesco Monticone, Le Quang Khai, Xing-Xiang Liu, Tom Hartsfield, Andrea Alu, **Xiaoqin Li**, “A subwavelength plasmonic metamolecule exhibiting magnetic based optical Fano resonance”, *Nature-Nanotechnology*, 8, 95, 2013

14. Jinwei Shi, Francesco Monticone, Sarah Elias, Yanwen Wu, Daniel Ratchford **Xiaoqin Li**, Andrea Alu, “Modular assembly of optical nanocircuits”, *Nature-Communications* 5, 3896, 2014
15. Akshay Singh, Galan Moody, Sanfeng Wu, Yanwen Wu, Nirmal J. Ghimire, Jiaqiang Yan, David G. Mandrus, Xiaodong Xu, and **Xiaoqin Li**, “Coherent Electronic Coupling in Atomically Thin MoSe₂”, *Phys. Rev. Lett.* 112, 216804, 2014
16. Yanwen Wu, Chengdong Zhang, Yang Zhao, Jisun Kim, Matt Zhang, N. Mohammadi Estakhri, Xing-Xiang Liu, Greg K. Pribil, Andrea Alù, Chih-Kang Shih, Xiaoqin Li, “Intrinsic Optical Properties and Enhanced Plasmonic Response of Epitaxial Silver”, *Advanced Materials* 26, 6106–6110, 2014
17. Kyongmo An, Daniel R. Birt, Chi-Feng Pai, Kevin Olsson, Daniel C. Ralph, Robert A. Buhrman, and **Xiaoqin Li**, “Control of propagating spin waves via spin transfer torque in a metallic bilayer waveguide” *PHYSICAL REVIEW B* 89, 140405(R) (2014)
18. Thomas Hartsfield, Wei-Shun Chang, SeungCheol Yang, Tzuhsuan Ma, Jinwei Shi, Liuyang Sun, Gennady Shvets, Stephan Link and **Xiaoqin Li**, “Single quantum dot controls a plasmonic cavity’s scattering and anisotropy”, *Proceedings of the National Academy of Sciences*, 112, 12288, 2015
19. Galan Moody, C. K. Dass, Kai Hao, Chang-Hsiao Chen, Lain-Jong Li, Akshay Singh, Kha Tran, Genevieve Clark, Xiaodong Xu, Gunnar Berghäuser, Ermin Malic, Andreas Knorr, **Xiaoqin Li**, “Intrinsic homogeneous linewidth and broadening mechanisms of excitons in monolayer transition metal dichalcogenides”, *Nature Communications* 6, 8315, 2015
20. Chun-Yuan Wang, Hung-Ying Chen, Liuyang Sun, Wei-Liang Chen, Yu-Ming Chang, Hyeyoung Ahn, **Xiaoqin Li**, Shangjr Gwo, “Giant colloidal silver crystals for low-loss linear and nonlinear plasmonics”, *Nature Communications* 6, 7734, 2015

B. Objective

Studies of light-matter interactions in quantum-confined systems and nanostructures have provided great insight into diverse and fundamental problems such as many-body interactions and entanglement. In particular, optical spectroscopy has proved

to be a powerful tool for elucidating electronic dynamics owing to its ability to access information that is difficult or impossible to obtain otherwise. The knowledge obtained from optical spectroscopic studies complement those obtained from other techniques and provide a more accurate picture of system dynamics. For example, electronic properties of materials are mainly determined by transitions within one energy band, which describe carrier transport in real space. On the other hand, optical properties are often related to transitions between valence and conduction bands. However, a strict separation between intraband and interband phenomena is impossible since both are simultaneously present and critical for determining the performance limit of future opto-electronic devices needed in DoD operations and future commercial products required by the society striving on modern technologies.

In the initial proposal, we outlined two specific projects: (i) investigation of coherent electronic coupling in semiconductor quantum dot clusters; (ii) investigation of spin wave dynamics in ferromagnetic multilayer structures. In the course of the project, we have expanded the first direction to include investigation of metallic nanoparticles and clusters as well as hybrid nanostructures consisted of both metallic and semiconductor components. In addition, we have studied an emerging class of atomically thin semiconductors known as the transition metal dichalcogenides. In this report, we summarize the key progress occurred during the past 6 years. These results have been broadly disseminated via conferences and scientific literatures. We choose a few representative examples to discuss in this technical report.

C. Scientific Accomplishments

We will focus on plasmonic and spin wave projects in this progress report on which we have made the most significant advance.

C.1 Plasmonic metamolecules exhibit tunable optical magnetic resonance

During 2013, we demonstrated a unique metamolecules that exhibit a strong magnetic dipole resonance that spectrally overlapped with the electric dipole. Such a metamolecule can be used as the basic building block for photonic materials with properties that do not exist in nature. Our work was published in Nature Nanotechnology. We describe the work in details below.

The lack of symmetry between electric and magnetic response in the optical frequency range is a fundamental consequence of the small value of the fine-structure constant and is directly related to the weakness of magnetic effects in optical materials^{1, 2}. Properly tailored plasmonic nanoclusters have been proposed to induce artificial optical magnetism³⁻⁶ based on the principle that magnetic effects are indistinguishable from specific forms of spatial dispersion of permittivity at optical frequencies⁷. In a different context, plasmonic Fano resonances have raised great

interest, particularly for use in sensing applications that benefit from sharp spectral features and extreme field localization⁸⁻¹². In absence of natural magnetism, optical Fano resonances have so far been based on purely electric effects. In this work, we demonstrate that a subwavelength plasmonic metamolecule consisting of four closely spaced gold nanoparticles (NPs) support a strong magnetic response coupled to a broad electric resonance. This finding represents an important step towards the quest for artificial magnetism and negative refractive index metamaterials at optical frequencies¹³⁻¹⁵.

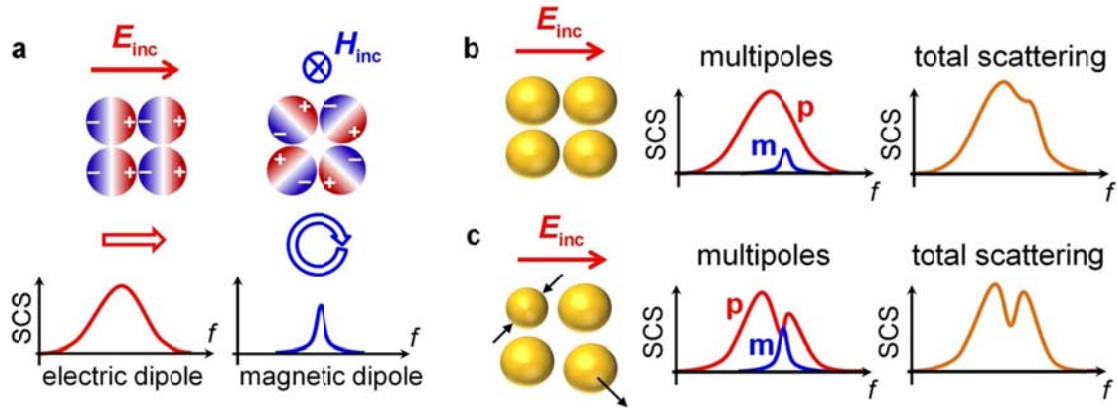


Figure 1. Illustration of the scattering response of plasmonic nanorings. (a) Scattering cross section (SCS) of a four-particle nanoring system excited by a time-varying electric field directed along the side of the square arrangement of particles (left) and by a time-varying magnetic field directed along the normal to the plane of the nanoring (right). Colors indicate the charge distribution inside each nanoparticle. (b) Scattering response of a symmetric nanoring and (c) when small asymmetries are introduced. Symmetry-breaking induces interference between the electric dipole (p) and magnetic dipole (m) modes, which gives rise to a pronounced Fano resonance in the scattering spectrum.

The key concepts are illustrated in Fig. 1: a perfectly symmetric nanoring (Fig. 1a) is designed to support overlapped electric and magnetic dipole resonances at visible frequencies¹². When excited by a local electric field, this geometry supports a broad electric dipole response. When excited by a local magnetic field, the induced circulating displacement current supports a sharper magnetic resonance centered in the same frequency range. In an ideally symmetric configuration, a time-varying electromagnetic wave would excite both orthogonal modes, which additively contribute to the total scattering cross section without interference (Fig. 1b). However, when small asymmetries are introduced, the modes lose their orthogonality and interfere, leading to a characteristic Fano dip in the electric dipole scattering signature due to magnetic resonance, reflected in the total scattering cross section (Fig. 1c).

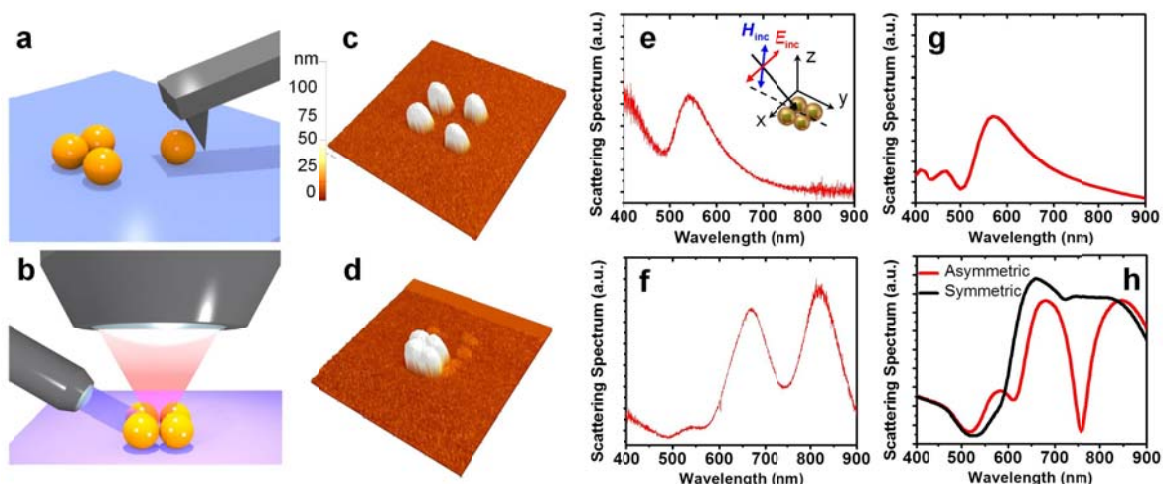


Figure 2. Experimental setup and scattering measurements vs. simulations demonstrating the presence of a magnetic-based Fano resonance in the asymmetric nanoring. Schematic representations of (a) AFM nanomanipulation and (b) optical scattering setup. (c) and (d) AFM images of the nanorings over 1.25 μm by 1.25 μm area. Measured scattering spectra (e) when the four nanoparticles are far apart and (f) when arranged in a square aggregation with small gaps. S-polarized incident light beam has been considered here. No analyzer was present along the collection path. (g) and (h) calculated total scattering cross section corresponding to the geometry in (c) and (d), respectively. Panel (h) compares calculated scattering cross sections for a perfectly symmetric nanoring and an asymmetric one.

We used AFM nanomanipulation to assemble the nanocluster, as illustrated in Fig. 2a. Initially, gold nanoparticles approximately 100 nm in diameter were randomly dispersed on a substrate. AFM was first used to image and identify the positions of several close-by nanoparticles. Next, four nanoparticles were assembled into a square geometry. Scattering measurements were taken using a home-built dark field microscope (Fig. 2b). As discussed above, the magnetic mode can couple to the electric mode due to suitable asymmetries, affecting the overall scattering signature, including the electric dipole component that our measurements directly observe. The scattering spectrum with no polarizer in the collection path (Fig. 2e) was dominated by a single, broad resonance centered at 540 nm, arising from the dipole resonance of the individual nanoparticles. When the gaps between the nanoparticles were decreased, a large red shift of the electric dipole resonance was observed (Fig. 2f) due to the increased capacitive coupling between neighboring nanoparticles. When the gap size was further reduced below 10 nm (AFM image in Fig. 2d), a pronounced dip centered at 740 nm was observed (Fig. 2f). This spectral feature, quite peculiar for such a subwavelength structure, corresponds to a Fano resonance, which originates from the interference between the radiant (bright), broad electric dipole and the sub-radiant (dark), narrow magnetic dipole modes as illustrated in Fig. 1c. This collective plasmon response can also be interpreted in

terms of hybridized states¹⁶, for which the interference between bonding and antibonding modes gives rise to the Fano resonance.

In order to confirm this intuitive interpretation of the observed spectrum, we performed numerical simulations using the three-dimensional finite element software COMSOL Multiphysics. The computed total scattering cross sections are displayed in Fig. 2g-h (red lines), showing good agreement with our measurements before and after the AFM assembly.

Our study convincingly demonstrates that a four-particle nanoring can support a strong optical magnetic resonance overlapped with a broad electric resonance. This specific geometry avoids radiative damping associated with higher-order scattering modes and boosts the magnetic response, despite the overall subwavelength size of the nanoring. In addition, the near-field interaction between the magnetic and electric modes, enabled by the small asymmetries in our geometry, has led to the first observation of a magnetic-based optical Fano resonance in the total scattering spectrum in a direction along which the direct magnetic response would otherwise be zero. Metamaterials with engineered electric and magnetic resonances and their controlled coupling may enable many fascinating applications in nanophotonics including cloaking, high resolution imaging, sensing and enhanced nonlinear optical response.

C.2 plasmonic orientation sensor

We have successfully demonstrated a new type of sensors that take advantage of near-field coupling to activate a dark mode in plasmonic NPs. This accomplishment resulted from the close collaboration between Prof. Li and Prof. Shvets' groups. We reported this result in a manuscript just published in Nature Photonics and two conferences.

A metallic nanoparticle (MNP) can enormously enhance the absorption or scattering cross-section of a barely visible emitting/scattering object (ESO) such as a molecule or a quantum dot placed in its close proximity. The near-field coupling between the ESO and the MNP underlying this enhancement has been exploited in applications ranging from surface enhanced Raman scattering^{17, 18} and fluorescence^{19, 20} to plasmonic sensors^{21, 22} and nanolasers²³⁻²⁵. It can also drastically modify the extinction spectrum of the resulting hybridized ESO/MNP nano-system and lead to Fano interference^{8, 26-33}.

Here, we introduce a novel concept, a plasmonic nano-protractor based on polarization spectro-tomography (PST) that exploits Fano interference to achieve three-dimensional super-resolution of an ESO placed in near-contact with an MNP. By utilizing a weakly scattering plasmonic nanorod as a “dark” ESO placed in close proximity with a “bright” MNP, we experimentally measure its three-dimensional position and orientation with respect to the MNP, as illustrated in Fig. 3. The nano-protractor can lead to breakthroughs in diffraction-unlimited, *in situ* imaging of complex molecules labeled by multiple ESOs. The idea of transducing changes in spatial arrangement between MNPs into spectral differences has been exploited in plasmonic rulers capable of measuring length variations in biomolecules^{34, 35} and nanoclusters³⁶. Here we coin the term “plasmonic nano-protractor” to highlight the new capability of our approach to pinpoint the spatial position and orientation of the ESO relative to the MNP. Our technique may be applied for studying *in situ* conformational changes such as rotation and bending at the single molecule level. Because multiple ESOs can have different resonant frequencies, this technique can be readily extended to super-resolution sensing of large molecules labeled by several distinct ESOs.

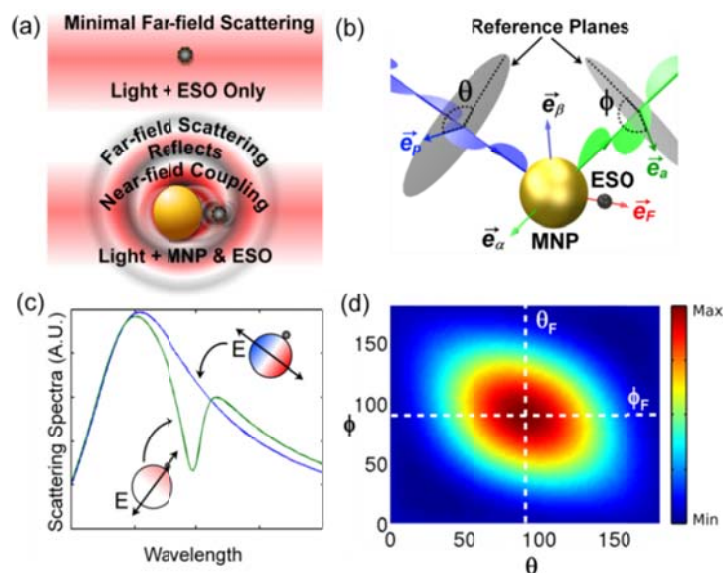


Figure 3: Conceptual schematics of the polarization spectro-tomography (PST) of a hybrid nano-object comprised of the “invisible” emitting/scattering object (ESO) and a large metallic nanoparticle (MNP). (a) The target ESO alone cannot be detected by light scattered in the far field due to its small scattering cross section. When coupled to a probe MNP in the near-field, the MNP/ESO hybrid produces strong scattered signal with characteristic asymmetric Fano lineshape. (b) Schematic of the proposed PST: the Fano axis of the MNP/ESO hybrid is uniquely determined by measuring the scattering spectrum for a range of polarizer (analyzer) angles, θ (ϕ). (c) The strength of the Fano resonance is strongly dependent on the polarization of the incident and scattered radiation. (d) A representative plot for a Fano-resonant polarizability of a MNP/ESO hybrid is used to identify the orientation of the Fano axis from the values of (θ_F, ϕ_F) .

To mimic a barely visible ESO, we used a gold nanorod which possesses a narrow “dark” resonance in the visible wavelength range corresponding to a quadrupole-like charge distribution as shown in Fig. 4a. While the stand-alone ESO was not detectable in the spectral range of the detector due to the small scattering cross section of the quadrupole resonance, the ESO/MNP hybrid was easily detected. Experimentally, the ESO (a gold nanorod with diameter $d \approx 22$ nm and length $L \approx 180$ nm) and the MNP (a gold sphere with diameter $D \approx 150$ nm) were brought together by pushing the nanosphere toward the nanorod using atomic force microscope (AFM) nanomanipulation³⁷⁻⁴⁰, as illustrated in Fig. 4b. Several consecutive steps of the manipulation process are shown in Fig. 4c. As the ligand-coated ESO and MNP were brought into near-contact, the scattering spectrum shown in Fig. 4d evolved from that of the isolated MNP (green line) to the asymmetric Fano-shaped spectrum of the ESO/MNP hybrid (blue line). The Fano resonance appeared near ~ 700 nm, which corresponds to the quadrupole mode of the nanorod. The precise alignment between the near-touching ESO and MNP can no longer be resolved by AFM imaging. Remarkably, such information can be obtained by applying the PST technique to the far-field scattering experiments as we demonstrate below.

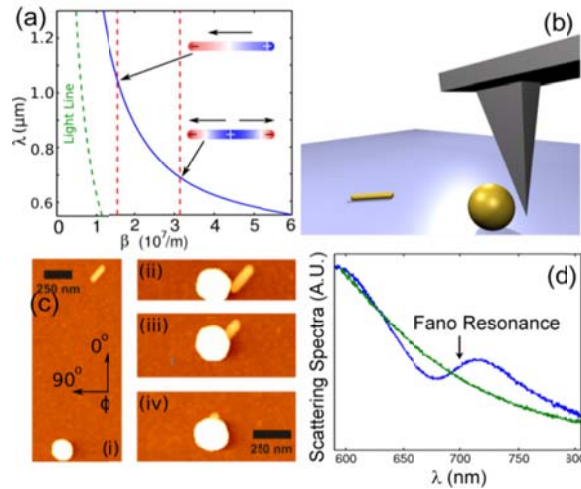


Figure 4: Optical resonances and experimental assembly of a MNP/ESO hybrid. (a) The dispersion relation (wavelength λ versus propagation wavenumber β) of the surface plasmons on an infinite gold wire with a 20 nm diameter. Fabry-Perot resonances of the finite length nanorod, $L = 180$ nm, are defined by the resonance condition $\beta \approx n\pi/L$ where $n=1$ (2) is the dipolar (quadrupolar) mode. (b) An illustration of the nanomanipulation method using AFM: the gold nanosphere (MNP) is brought in contact with a gold nanorod (ESO). (c) AFM images of the nanosphere and nanorod at different steps (i-iv) in the assembling process; (d) The scattering spectra of the MNP measured before (green) and after (blue) the ESO was brought into contact. A Fano resonance emerged at $\lambda \approx 700$ nm after the assembly was completed.

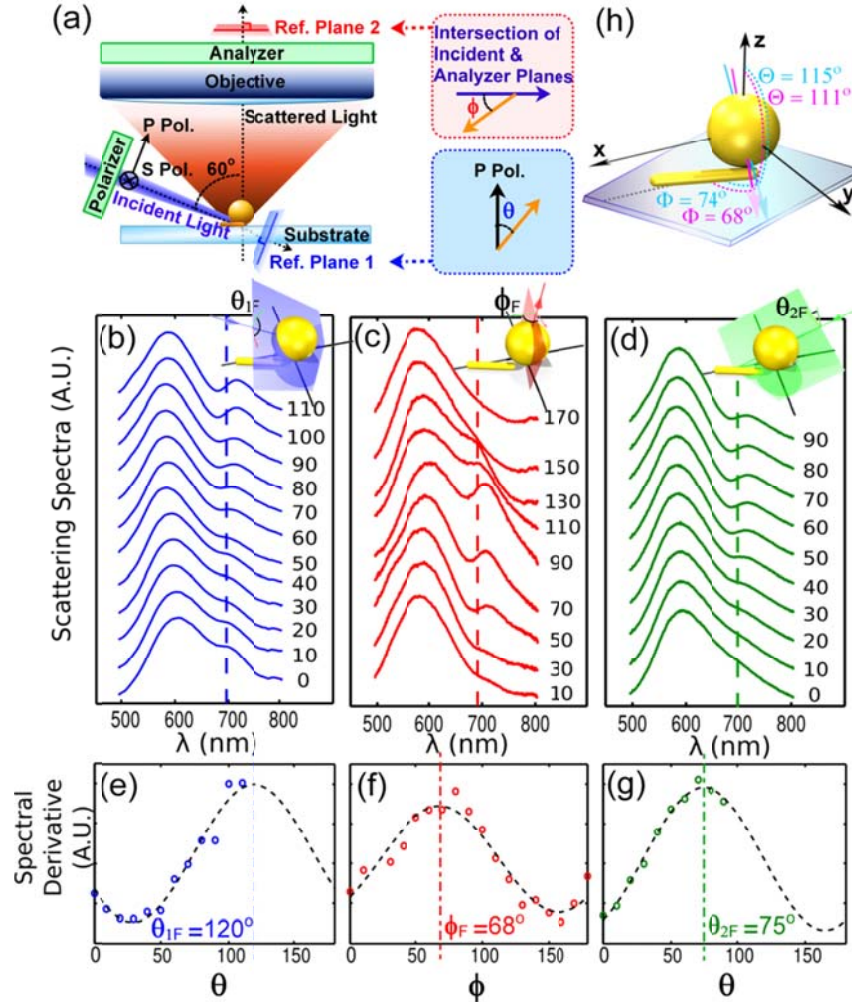


Figure 5: Experimental data of PST on the MNP/ESO hybrid comprised of the plasmonic nanosphere and nanorod. (a) Schematics of the experimental set-up and the reference axes; (b-d) Measured scattering spectra for varying values of the polarization angle, θ , of the incident light and for varying values of the analyzer angle, ϕ , of the scattered light with p-polarized ($\theta = 0$). The sample was rotated 180° around the substrate normal between (b) and (d). (e-g) Spectral derivatives $\bar{D}_{1,2}(\theta)$ and $\bar{D}_1(\phi)$ taken at the wavelength indicated by the dashed line in (b-d) as a function of the polarizer/analyzer angle. The shaded planes in the insets of (b-d) are defined by the Fano axis projections and the incident beams as in (b) and (d) or by the Fano axis projection and the substrate normal as in (c). (h) Determination of the Fano axis by combining either θ_{1F} with ϕ_F (approach 1) or θ_{2F} with ϕ_{2F} (approach 2 and substrate).

The experimental set-up for the PST measurements and the definition of the polarization angles are illustrated in Fig. 5a and explained in the caption. For convenience, θ/ϕ in the polarizer/analyzer reference planes were defined as follows: $\theta = 0^\circ$ direction corresponds to the p-polarization of the incident beam, and $\phi = 0^\circ$ corresponds to the intersection between the incident plane and the substrate. The total *unpolarized* scattering spectra $\bar{I}_1(\lambda; \theta) \equiv \langle I(\lambda; \theta, \phi) \rangle_\phi$ shown in Fig. 5b were measured as a function of the polarizer angle θ and wavelength $\lambda \equiv 2\pi c/\omega$. The

second set of spectra $\bar{I}_2(\lambda; \theta)$, shown in Fig. 5d, correspond to the light incident from the opposite side of the assembled structures while preserving the same incidence plane. This set of data was taken by rotating the sample by 180° around the substrate normal. From here on, subscripts 1 and 2 refer to the two sample orientations. Finally, the *polarized* scattering spectra, $\tilde{I}_1(\lambda; \phi) \equiv I(\lambda, \theta = 0, \phi)$ were measured as a function of the analyzer angle, ϕ , using *p*-polarized incident light as shown in Fig. 5c.

The magnitude of the Fano feature is quantified by the derivative of the scattering spectra evaluated at the Fano resonance wavelength λ_R . The spectral derivatives, $\bar{D}_{1,2}(\theta) = \partial \bar{I}_{1,2}(\lambda; \theta) / \partial \lambda|_{\lambda=\lambda_R}$ and $\tilde{D}_1(\phi) = \partial \tilde{I}_1(\lambda; \phi) / \partial \lambda|_{\lambda=\lambda_R}$ are plotted in Fig. 5e-5f. The spectral derivatives reach their maximal values when the angles of the polarizer and analyzer are aligned with the projections of the Fano axis in the respective reference planes. By fitting harmonic functions to Fig. 5e-5g, we extracted the angles corresponding to the maximal spectral derivatives as $\theta_{1F} = 120^\circ \pm 5^\circ$, $\phi_F = 68^\circ \pm 5^\circ$, and $\theta_{2F} = 75^\circ \pm 4^\circ$. Any two of these three angles can be used to define the Fano axis.

As the insets in Fig. 5b-5d demonstrates, the Fano axis direction can be geometrically defined by the intersection of two planes. We used two different approaches to explicitly reconstruct the Fano axis. In the first approach, we combined θ_{1F} and ϕ_F , where one plane is defined by the polarization direction of $\theta_{1F} = 120^\circ$ and the incident beam direction, and another defined by the analyzer direction of $\phi_F = 68^\circ$ and the substrate normal. The same procedure was used to reconstruct the Fano axis direction using θ_{1F} and θ_{2F} in the second approach. We now specify the Fano axis in the lab frame, as defined in Fig. 5h, to facilitate direct comparisons between the two approaches. In this lab frame, the Fano axis direction extracted from the first (second) approach corresponds to $\Theta = 111^\circ, \Phi = 68^\circ$ ($\Theta = 115^\circ$ and $\Phi = 74^\circ$) as indicated by the cyan (magenta) lines in Fig. 5h. Here (Θ, Φ) are the standard spherical coordinates. Note that the Fano axis extracted from these two independent approaches agrees within the experimental errors, thereby providing the key experimental confirmation of the PST technique introduced in this work. Below we demonstrate how the Fano axis direction can be used to determine physically relevant quantities such as the nanorod/nanosphere contact point and the relative nanorod orientation. In another recent experiment, we have extended this plasmonic protractor concept to a system consisted of a plasmonic nanosphere and a single semiconductor dot. In that case, the Fano resonance is mediated by single photon absorption events. The Fano resonance is present even when the QD has already photobleached because of its still intact ability to absorb photons.

C.3 Progress on Plasmonic circuit project

We experimentally demonstrated that circuit concepts can be used to model photonic components, extending the powerful concept of modular and lumped elements from electronics to photonics. This work was published in Nature Communication in 2014.

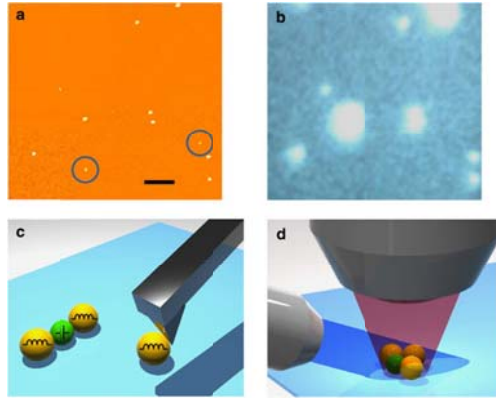


Figure 6: **Assembly and characterization of a modular optical nanocircuit.** (a) AFM and (b) dark-field scattering images of plasmonic and dielectric NPs randomly distributed on a glass substrate. Only Au NPs yield strong scattering signals. Scale bar, 3 μm . The NPs enclosed in circles in a are missing in b, thereby identifying them as dielectric NPs. (c) Illustration of AFM nanomanipulation as a way to dynamically assemble complex optical nanocircuits from independent optical inductors (plasmonic NPs, yellow) and capacitors (dielectric NPs, green). (d) Schematic representation of our dark-field scattering measurements. Light impinges at an incidence angle of 60 degrees and the scattering signal is collected along the substrate normal.

Here we employ small colloidal metallic and dielectric nanoparticles (NPs), ideal platforms to translate these concepts to nanophotonic systems. With optical nanocircuit concepts⁴¹⁻⁴⁴, we are able to control the intrinsic optical impedance of NPs by their geometry and material composition. This impedance is defined as the ratio of the local potential difference $V=|E|\cdot L$ and the flux of displacement current $I_d=-i\omega|E|S$ through the NP⁴¹⁻⁴⁴, where E is the local electric field vector, L is the NP length along the electric field, ω is the frequency of operation, ϵ is the NP dielectric constant and S is its transverse cross-section. It follows that a dielectric NP with $\text{Re}(\epsilon) > 0$ behaves as a nanocapacitor, while a metallic NP with $\text{Re}(\epsilon) < 0$ acts as a nanoinductor. Ohmic loss in the materials takes the role of a nanoresistor.

In this experiment, gold NPs (~ 60 nm in diameter) and Al_2O_3 NPs (~ 45 nm in diameter) were dispersed on a glass substrate. The AFM image of the sample (Fig. 6a) allowed us to locate each NP but did not distinguish between different NP types without ambiguity. Then we mapped the same area using optical dark-field microscopy, from which only scattering signals from Au NPs were detectable (Fig. 6b). Correlating the AFM and optical scattering images allowed us to differentiate metallic NPs

(nanoinductors) from dielectric NPs (nanocapacitors) with certainty. By measuring the scattering from each NP, we detected differences in the scattering spectra because of slight variations in NP shape and size. We then picked a few chosen NPs with the desired impedance and assembled them to produce more complex connections (Fig. 6c) using the AFM tip. Finally, dark-field scattering measurements, shown schematically in Fig. 6d, were used to confirm the functionality of the nanoclusters by comparing the measured scattering spectra with the predicted nanocircuit response.

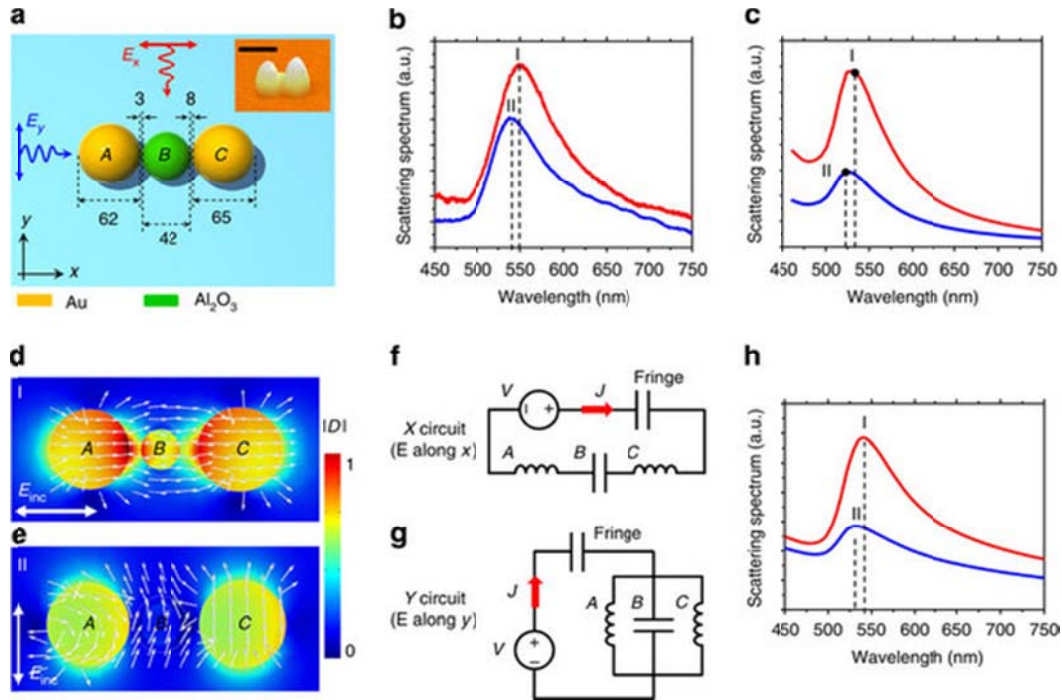


Figure 7: Second and third order lumped nanofilters. (a) AFM image and geometry of a 3-NP cluster composed of an Al_2O_3 NP sandwiched between two AuNPs. All dimensions are in nanometres. Scale bar, 100 nm. (b) Dark-field scattering measurements for s-polarized light exciting the nanocircuit with the electric field along x (red line) or y (blue). (c) Corresponding full-wave simulations with electric field along x (red line) or y (blue). (d,e) Simulated electric displacement field distributions and field vectors at the resonance wavelengths for the two incidence directions: $\lambda = 532$ nm (d) and $\lambda = 524$ nm (e). (f,g) Thevenin nanocircuit models of second order and third order lumped nanofilters. (h) Corresponding circuit theory predictions: X-circuit (red line) and Y-circuit (blue).

We first consider a three-particle nanocircuit consisting of a dielectric Al_2O_3 NP sandwiched between two Au NPs, as shown in Fig. 7a. The measured scattering spectra from this nanocluster using s-polarized light are shown in Fig. 7b, with the incident electric field either perpendicular to the NP array (Y-circuit, blue line) or along it (X-circuit, red line). Owing to the anisotropy of this nanocluster, the optical response exhibits a spectral shift dependent on the direction of the impinging field relative to the NP array. A red shift in resonant wavelength is expected for the X-circuit (Fig. 7b),

which agrees with full-wave simulations (Fig. 7c). Figure 9d,e shows the corresponding simulated displacement vector distributions at the two resonant wavelengths: $\lambda=532$ nm for incident electric field parallel to the x axis (Fig. 7d) and $\lambda=524$ nm for electric field along the y axis (Fig. 7e). Similar to a conventional electronic circuit, the intrinsic nanoinductance of the gold NPs is not affected by other components in the circuit.

On the basis of the different electric displacement field distributions (Fig. 7d,e), two circuits with different connections among the elements (Fig. 7f,g) account for the change in the scattering spectra. The three nanocircuit elements are connected in series (X-circuit in Fig. 7f) for incident electric field polarized along the axis of the NP cluster, since this excitation ensures the continuity of the displacement current across the cluster, as confirmed by our simulations in Fig. 7d. In conventional circuit theory, the number of independent reactive elements determines the order of a filter. Accordingly, the X-circuit (Fig. 7f) realizes a second order filter, which is an LC circuit formed by the series combination of an inductor (the Au NPs) and a capacitor (determined by the Al_2O_3 NP and the fringing fields). Conversely, for incident electric field perpendicular to the axis of the NP cluster (Fig. 7e), each element experiences the same potential difference (that is, voltage), leading to a parallel connection between them. This Y-circuit (Fig. 7g) forms a third order nanofilter, in which the fringe capacitance is connected in series to the parallel of the Au NP inductors and the Al_2O_3 NP capacitor. The scattering spectra predicted by our circuit model (Fig. 7h) are indeed quantitatively consistent with the measured and simulated spectra for both X- and Y-circuits (Fig. 7b,c). By realizing different circuit configurations controlled by the direction of the excitation field, we are able to experimentally prove the design and operation of optical stereo-circuits, which do not have a counterpart in the electronic realm.

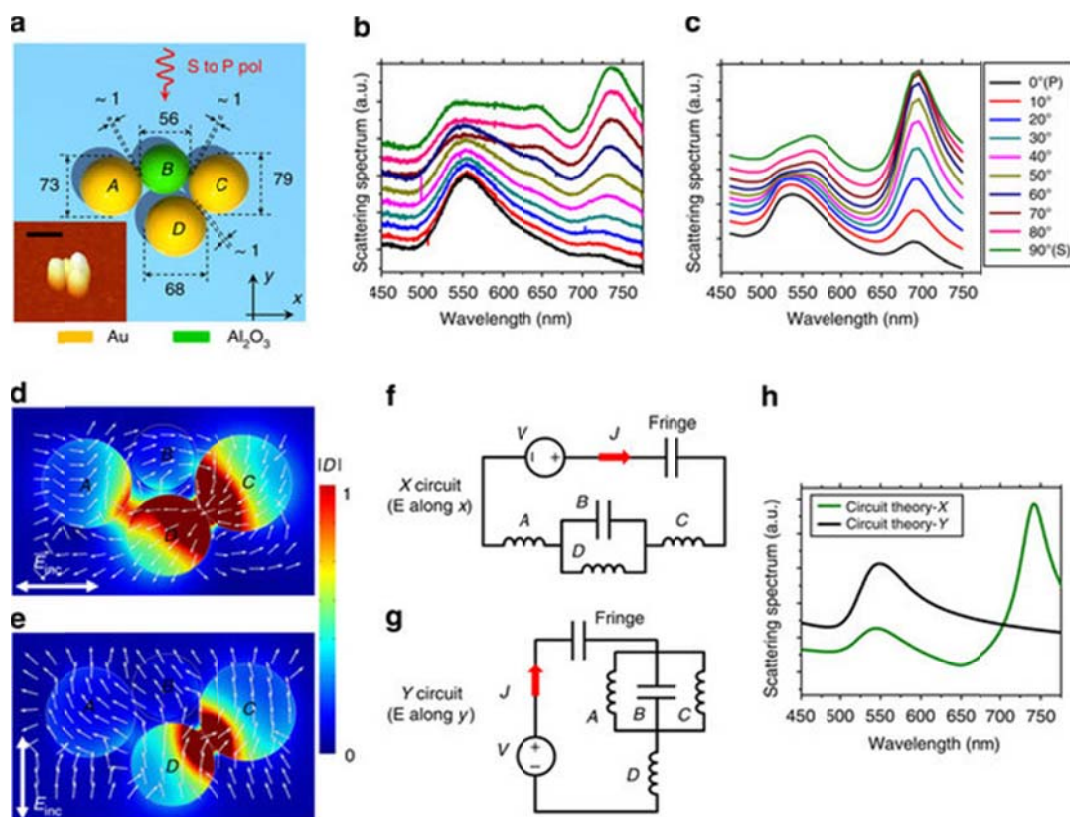


Figure 8: A fourth order lumped nanofilter.(a) AFM image and geometry of a 4-NP complex nanocircuit composed of three Au NPs and one Al₂O₃NP. All dimensions are in nanometres. Scale bar, 100 nm. (b) Dark-field scattering measurements for polarization rotating from s to p; (c) corresponding full-wave simulations. Curves in b,c have been shifted vertically to facilitate comparisons. (d,e) Simulated electric displacement field distributions and field vectors for polarizations parallel (d) and orthogonal (e) to the array axis, at the $\lambda=688$ nm. (f,g) Thevenin nanocircuit models. (h) Corresponding circuit theory predictions for the two orthogonal polarizations.

Then we further add another metallic NP below the previous nanocircuit design, as illustrated in Fig. 8a. The scattering measurements shown in Fig. 8b were taken with incident light direction fixed while gradually changing the polarization from p to s. Our experiments (Fig. 8b) agree well with full-wave simulations (Fig. 8c). Shown in Fig. 8d,e are the simulated displacement vector distributions at the longer wavelength resonance ($\lambda=688$ nm), for polarizations parallel (Fig. 8d) and orthogonal (Fig. 8e) to the array, highlighting the polarization-dependent interaction among NPs. Even in this more complex configuration, the electric displacement vector distributions fully support the circuit models reported in Fig. 8f,g, which correspond to fourth order nano-filters. This example shows that we can quantitatively control the spectral response by connecting an additional nanoinductor. More specifically, we have been able to add a new zero and/or pole to the scattering response by adding an independent reactive element to the circuit of Fig. 7. Rather than modeling a distributed photonic system with an equivalent

circuit⁴⁵⁻⁴⁷, our work shows that it is actually possible to synthesize photonic circuit functionality by assembling modular lumped elements.

We would like to emphasize the key message of this work: the nanocircuit paradigm provides an unmatched degree of simplicity to control and tailor the optical response of rather complex nanophotonic structures. Remarkably, the impedance of each nanosphere remains independent of the cluster geometry and surrounding environment in all the circuits we have demonstrated, starting from the isolated NP to the complex fourth order nanocircuit. In other words, each NP carries inherent optical impedance, which is a property of the particle itself, allowing us to modularize its response and combine it in complex configurations.

C.4 Progress on plasmonic nanoparticle-quantum dot hybrid structure

We experimentally demonstrate for the first time that a single semiconductor quantum dot placed in nanometer-scale proximity of a plasmonic cavity can be used to control the scattering spectrum and anisotropy of the latter. This work was published in Proceedings of the National Academy of Sciences in 2015.

Many quantum network and information processing schemes require the enhanced light-matter interaction between a single quantum emitter and a cavity, enabling the effective conversion between photonic and matter-based quantum states⁴⁸⁻⁵¹. Those cavity-quantum electrodynamics (QED) effects require a high Purcell factor $F_p \propto Q/V$, where Q is the quality factor, and V is the volume of the cavity mode⁵². The high Q of conventional photonic cavities is required to compensate for relatively large (diffraction-limited) mode volumes and comes at a cost: the narrow linewidth of cavity modes places stringent requirements on their spectral alignment with the frequencies of quantum transitions. Plasmonic cavities, on the other hand, achieve high values of F_p while maintaining moderate Q values because of their ultra-small modal volume. The relaxed spectral alignment requirements facilitate the experimental realization of various quantum phenomena, such as collective photon emission from a small ensemble of emitters⁵³ and single photon sources with tunable statistical properties⁵⁴.

Prior experiments exploring cavity QED effects associated with single emitters coupled to plasmonic cavities or waveguides focused almost exclusively on the observations of reducing the emitter's lifetimes^{19, 55, 56}. The realms of quantum information science and plasmonics have also been bridged by demonstrating that photon emission statistics, such as anti-bunching behavior in the second order correlation function for single photon sources, remain intact following the photon-plasmon-photon conversion process⁵⁷⁻⁵⁹. The possibility of controlling the scattering of

a plasmonic nanocavity by a single (and inherently quantum and nonlinear) two-level system has also been proposed^{54, 60, 61} but never experimentally observed.

The strongly coupled MNP-QD hybrid structure is assembled into a well-controlled geometry using the technique of AFM nanomanipulation. The strong coupling between the MNP and QD is experimentally confirmed by measuring the exciton lifetime. Analyzing the polarization and spectral properties of light scattered by the MNP-QD hybrid, we observe that the overall plasmonic cavity scattering is significantly modified over a broad spectral range. A Fano resonance spectrally aligned with the QD's quantized exciton resonance is clearly identified when the polarization of the scattered photon is along the Fano axis⁶² connecting the MNP's center with the QD. The anisotropic scattering spectrum observed in our experiments suggests that a polarization-controlled, versatile quantum light source may be realized in this simple QD-MNP cavity system.

The calculated polarization-resolved scattering spectra by the QD-MNP (diameters: $2r_{QD} = 6\text{ nm}$ and $2r_{MNP} = 30\text{ nm}$) hybrid are shown in Fig.9(a) for three polarization angles ϕ_A of the analyzer placed in the collection path of the scattering signal to mimic the experimental setup. In the absence of the QD, all scattering spectra from a single MNP are independent of ϕ_A and possess a single broad peak at $\lambda_{MNP} \approx 520\text{ nm}$ corresponding to the plasmonic dipole resonance of the MNP. The introduction of a QD under the MNP, with the separation gap of $g = 1\text{ nm}$, modifies the scattering spectrum: a sharp Fano feature emerges at the exciton transition wavelength $\lambda_{QD} = 550\text{ nm}$. The magnitude of the feature is a strong function of the analyzer orientation. If the projection of the Fano axis onto the analyzer plane is perpendicular to the analyzer direction ($\phi_A = \pi/2$ in Fig.9(a)), then no Fano feature is predicted by our calculation. The strongest Fano feature is observed for $\phi_A = 0$, and a weaker but finite Fano feature is observed for intermediate angles. Therefore, what is originally an isotropic scatterer (a spherical MNP) is transformed into a highly anisotropic one by the strong hybridization between the QD and the MNP.

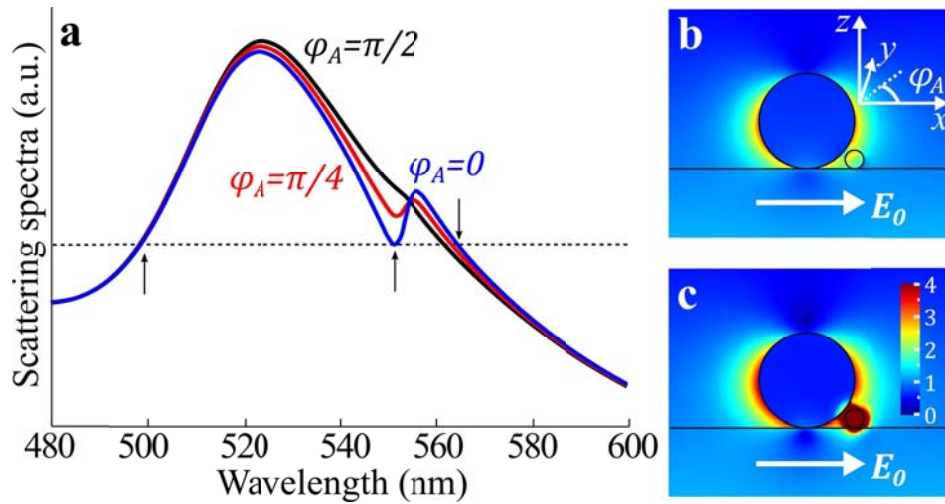


Fig 9: Calculation demonstrating how the near-field coupling modifies the far-field scattering spectra of a NP-QD hybrid structure placed on a glass substrate.(a) The scattering spectra of a NP-QD hybrid excited by the unpolarized evanescent wave coming from the glass substrate side in all azimuthal angles. The angle φ_A indicates the orientation of the analyzer in the path of the scattered light. Fano feature is the most (least) prominent when the orientation of the analyzer is parallel (perpendicular) with the in-plane component of the Fano axis, which connects the QD and MNP centers. (b) and (c) shows the field near the NP-QD hybrid at 500 nm and 552 nm, respectively, as indicated by the black arrows in the scattering spectrum at $\varphi_A = 0$ in (a). The scattering signal at these two wavelengths is the same (indicated by the dotted line on the blue curve) while the MNP is excited much more strongly in Fig 1c. This wavelength dependence proves that the presence of the QD indeed controls the MNP's scattering and anisotropy resonantly.

The ability of a single QD to modify the scattering spectrum of a much larger MNP possessing a scattering cross section of $(r_{\text{MNP}}/r_{\text{QD}})^6 \approx 15,000$ -fold greater in magnitude than that of the QD seems surprising. Naively, one may expect the effect of a QD on the scattering spectrum of the hybrid system to be very small. As pointed out by a number of theoretical studies^{54, 60, 61} and our own numerical calculation shown in Fig. 9, this expectation is not correct. While the exciton dipole moment is too small to produce significant far-field scattering on its own, it is sufficient to de-polarize the MNP in the near-field, thereby dramatically modifying the electric polarizability of the combined hybrid system at the frequency of the exciton transition.

To illustrate this point, the near-field distributions were calculated for $\lambda_1 = 500$ nm (Fig. 9b) and $\lambda_2 = 552$ nm (Fig. 9c), respectively. These two wavelengths were chosen because the scattering intensities are the same. The much higher (by almost a factor of 2) electric field induced on the MNP's surface at $\lambda = \lambda_2$, is offset by strong near-field depolarization (light-color area near the QD) of the MNP by the exciton's dipole. Because the electric field of a dipole rapidly decays with distance, such extreme depolarization (which can be alternatively interpreted as the excitation of high-order multipoles of the MNP by an exciton) can only occur if the QD is placed within nanometers from the MNP. Therefore, it is extremely crucial to precisely position the QD near the MNP as accomplished in our experiments.

We assemble the hybrid structure using the technique of AFM nanomanipulation^{39, 63, 64}. The assembly process begins by dispersing MNPs and QDs on a glass substrate randomly. We then simultaneously obtain an AFM topography image and a photoluminescence (PL) image by scanning the sample on a home-built integrated AFM-confocal microscope. We locate isolated MNPs and QDs in close proximity via the AFM topography image. We then manipulate a near-by MNP to approach the chosen QD. We then measure the lifetime to confirm that the MNP is indeed in the close proximity of the QD. Lifetime is, in fact, a rather accurate way to characterize the distance between the MNP and QD as demonstrated in our previous work⁶⁵.

Measured ensemble absorption and PL emission spectra (taken in solution) of QDs are shown in Fig. 10b. The absorption spectrum features multiple discrete exciton resonances at lower energies and a continuous absorption spectrum at energies above the band gap of the crystal. While all absorption resonances may influence the scattering spectrum of the hybrid structure, we focus on the lowest-energy exciton state centered near $\lambda_{QD} \approx 615$ nm with an ensemble-averaged spectral full-width at half-maximum (FWHM) $\Delta\lambda_{1/2} \sim 15$ nm.

The dark-field scattering experiments are performed using a home-built optical system optimized for small MNP measurements (Fig. 10a). An un-polarized white light source incident in a conical geometry generates evanescent fields and excites the hybrid structure from all directions. An analyzer is placed in the scattered light's path to select the polarization of the collected scattering. A series of such spectra are displayed in Fig. 10c as a function of the analyzer angle. A very sharp Fano feature can be clearly observed for $\phi_A = \phi_1 = 30^\circ$. Weaker Fano features are observed for other polarizer orientations, all in qualitative agreement with our theoretical predictions in Fig. 9a.

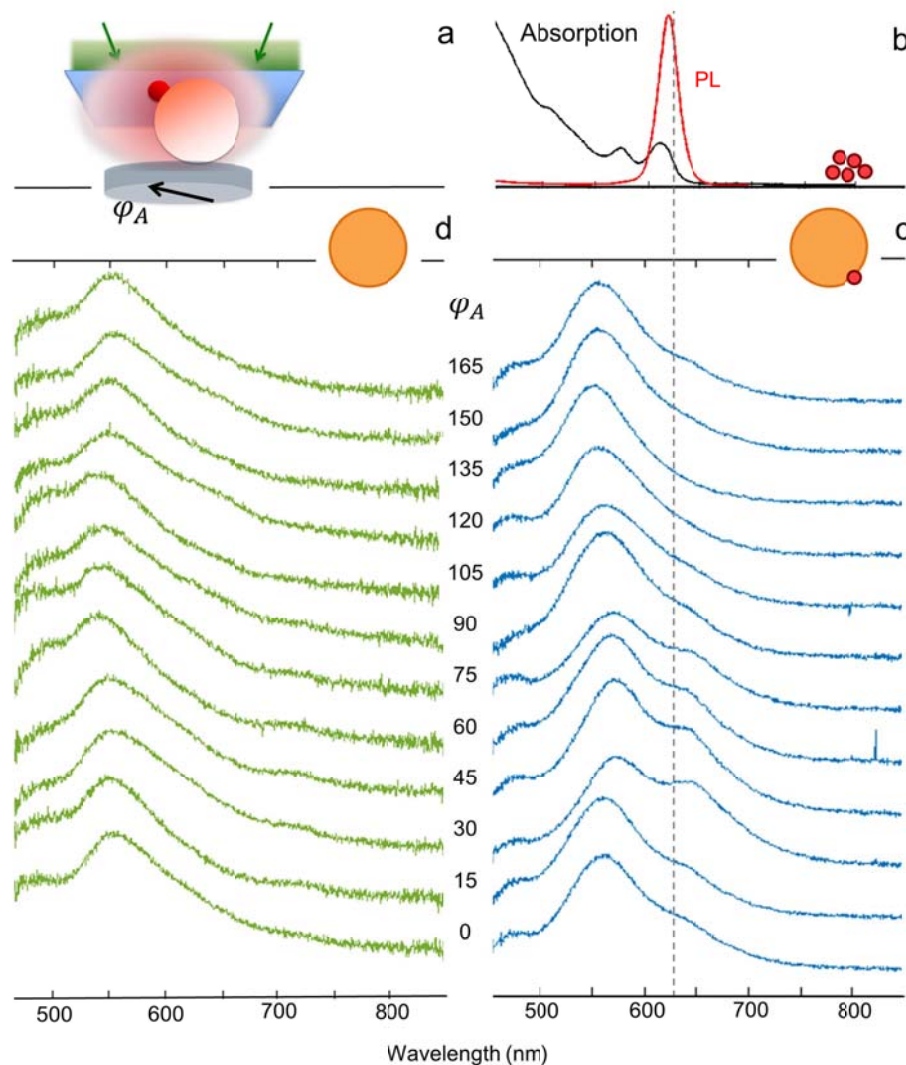


Fig. 10: The scattering and anisotropy of a plasmonic cavity (i.e. a MNP) controlled by a single QD. (a) Experimental schematics for scattering measurements; (b) Experimentally measured absorption (black) and PL emission (red) spectra from an ensemble of colloidal CdSe/ZnS core-shell QDs. (c) Measured scattering spectra of the assembled QD-MNP hybrid structure at different analyzer angles. The Fano resonance indicated by the dotted vertical line spectrally aligns with the lowest exciton state measured in the absorption from an ensemble of QDs. The Fano resonance is most pronounced at $\phi_A = 30^\circ$. (d) Measured scattering spectra of a bare 30 nm diameter MNP at different analyzer angles. The small changes near 550 nm or below are likely due to deviations from a perfectly spherical shape of the MNP.

To further confirm that the polarization dependence in the scattering spectra of the hybrid structure indeed originates from the coupling between the QD and MNP, we show the scattering spectra of a bare MNP in Fig. 10d. The spectra do not display any

Fano features or analyzer angle dependence in the spectral proximity of the exciton resonance λ_{QD} . Therefore, it is indeed the coupling between a single QD and the MNP that turns an otherwise isotropic plasmonic cavity into a strongly anisotropic one. Because a single quantum absorber achieves this effect, one can envision the proposed hybrid system as an experimental platform for observing a plasmonic cavity anisotropy controlled by optical nonlinearity at the single-photon level. The small angular variations of $S(\lambda, \phi_A)$ at shorter wavelengths (around 550nm or below) in Fig. 10c and Fig. 10d most likely arise from a small intrinsic deviation of the MNP's shape from an ideal sphere. Unlike the extrinsic anisotropy induced by the QD, it cannot be optically controlled and is not of interest for nonlinear quantum optics.

In summary, we have demonstrated that a single semiconductor QD coupled to a MNP cavity can effectively control the scattering spectrum of the latter, as well as render it highly anisotropic. The speculative implications of such extrinsic anisotropy are very intriguing. On the one hand, it serves as an orientation sensor to determine the relative locations of the QD and MNP. On the other hand, it should be possible to observe polarization-dependent photon statistics of light scattered from the QD-MNP nano-hybrid.

C.5 Re-Examine Fundamental Optical Properties of Silver

In this work, we explore the intrinsic fundamental optical properties of Ag. Using atomically smooth epitaxial Ag films, we extracted new optical permittivity highlighting significant loss reduction in the visible frequency range. This work was published in Advanced Materials in 2014.

Loss represents the most serious challenge that impedes progress and broad impact towards practical technology in the field of plasmonics⁶⁶⁻⁶⁸. Silver (Ag) is by far the preferred plasmonic material at optical frequencies due to its lowest loss among all metals. However, large discrepancies exist among widely quoted values of optical permittivity in Ag due to variations in sample preparation. Here we push to the limit of intrinsic fundamental optical properties of Ag. We extracted new optical permittivity highlighting significant loss reduction in the visible frequency range from atomic smooth silver film. We measured a largely enhanced propagation distance of surface plasmon polaritons (SPPs), which confirmed that the intrinsic loss in Ag is lower than previously considered possible. The new optical constants are free of extrinsic spectral features typically associated with grain boundaries and localized plasmons inevitably present in thermally deposited films.

In this work, we performed careful spectroscopic ellipsometry (SE) measurements and analyses on atomically smooth, epitaxially grown, single crystalline Ag films⁶⁹⁻⁷¹, and accurately extracted Kramers-Kronig (K-K) consistent optical constants. Our

measurements suggest that the intrinsic loss in *Ag* is significantly lower, by up to a factor of 2 in the visible wavelength range, than the best values previously reported by JC⁷². We also measured SPP propagation distances along these epitaxial *Ag* films, finding greatly enhanced propagation lengths, approaching the fundamental limit determined by the new optical constants at both visible and near-infrared (NIR) frequencies. The measured propagation distance confirms that the loss determined from the permittivity data reported by JC is not an intrinsic limit.

Atomically smooth *Ag* films were grown using molecular beam epitaxy (MBE) on heavily doped Si(111)-7×7 substrates. The high surface quality of a 45 nm oxide capped epitaxial film was confirmed by atomic force microscopy (AFM) shown in Fig. 11a. For comparison, a 50nm thermally deposited film was also scanned, as shown in Fig. 11b. The evaporated film has a root mean square (RMS) roughness of 3.27 nm while the epitaxially grown film has a roughness of only 0.36 nm, nearly an order of magnitude smaller. Low-energy electron diffraction (LEED) and reflection high-energy electron diffraction (RHEED) patterns shown in Fig. 11c and 11d, respectively, taken *in-situ*, further confirm the long-range single crystalline nature of these films.

We performed SE measurements and analyses⁷³⁻⁷⁵, to multiple epitaxial and thermal silver films. We present here results from three representative films: an uncapped 40 nm epitaxially grown film, a 45 nm epitaxial film capped with 1.5 nm of *MgO* and 2 nm of *Al*₂*O*₃, and an uncapped 50 nm thermal film deposited at a rate of 0.35 nm/s serving as control. The *MgO/Al*₂*O*₃ cap is a crucial element to prevent the rapid degradation of epitaxial silver due to surface oxidation in ambient conditions, and we confirmed via SE measurements that the *Ag* film's pristine quality persists even after capping. In our fitting, we used simple *Ag/Si* or *capping/Ag/Si* structural models for the epitaxial films as shown in Fig. 11e. The fitted result for ϵ_2 from each film is plotted against those for a 40 nm thermally deposited film measured by JC and the data compiled by Palik from multiple samples. In this work, we concentrate on the energy range below the interband transition threshold, which is relevant to most plasmonic applications.

In the energy region below 3.8 eV, the contribution to ϵ_2 mainly comes from intraband transitions typically accompanied by scattering between electrons, lattice vibrations (phonons), surface roughness and grain boundaries inside the bulk. Since epitaxially grown films are single crystalline, scattering from imperfections is expected to be lower than that in thermal films. Our measurements indeed show significantly lower loss than JC's values in the 1.8-2.5eV range, while the control film shows values in between JC and Palik data. The residues in this region are small and centered around zero for all films, suggesting that our model fits the data very well. In the lowest energy range below 1.5 eV, the error becomes large due to reduced detector efficiency and our extracted ϵ_2

appears to be larger than that reported by JC. We note that the original JC data contain large errors in this same energy region (gray shadow in the Fig. 11f-1h). Thus our measurements are consistent with JC's in this lowest energy region.

The residues shown in Fig. 11f-1h are not completely random: on close inspection, in the energy range near 3.7 eV, indicated by the orange circle in all panels, one can see a sizable peak in the residue for the thermal film (Fig. 11h) that is absent in both epitaxial films (Fig. 11f and g). We suggest that this peak is associated with the presence of grain

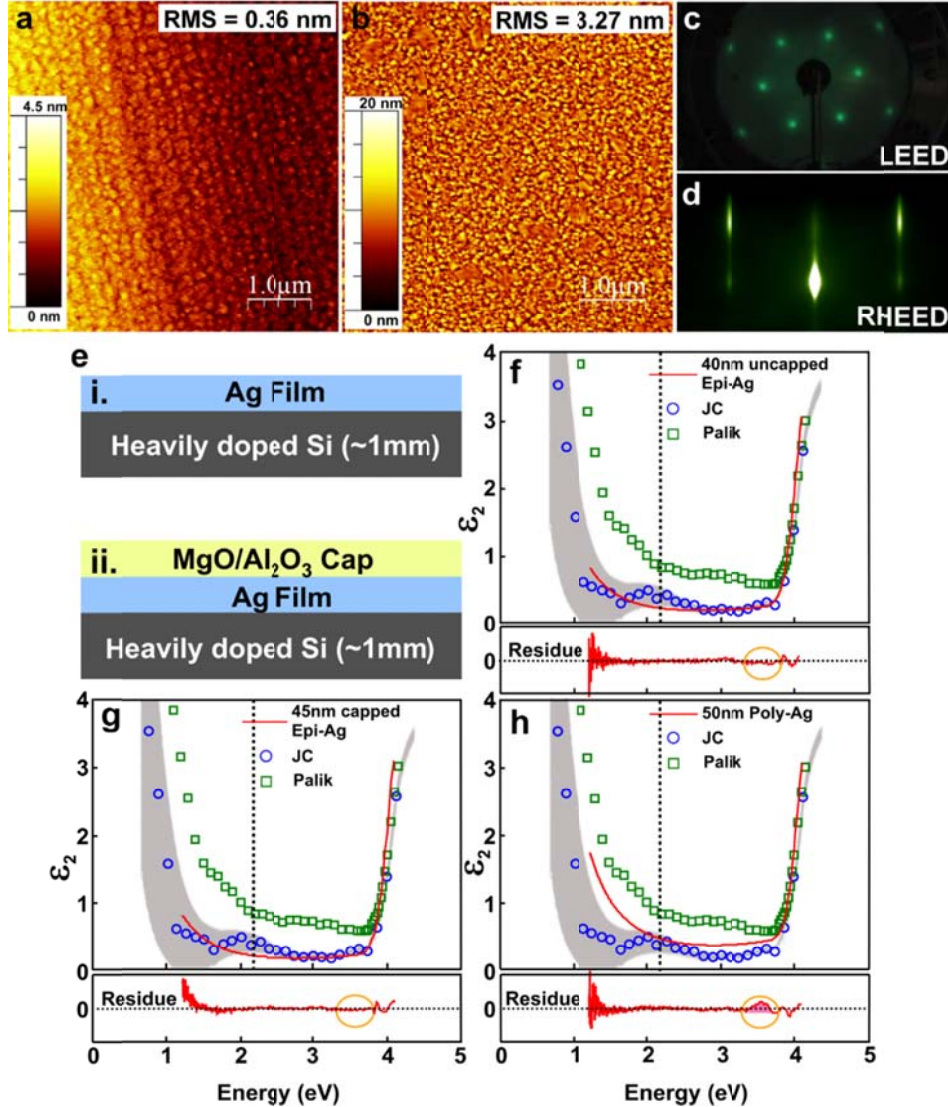


Fig. 11. AFM scans of (a) a 45 nm epitaxial (2 nm Al₂O₃/1.5 nm MgO capped) and (b) a 50 nm thermally deposited (0.03 nm/s deposition rate) Ag film. (c) LEED and (d) RHEED patterns of an epitaxially grown Ag film. (e) Layered structures of our Ag film samples with and without oxide capping. Energy dependence of ϵ_2 extracted from SE measurements on (f) an uncapped 40 nm epitaxial film, (g) a 45 nm epitaxial film capped with 1.5 nm of MgO and 2 nm of Al₂O₃, and (h) an uncapped 50 nm thermal film deposited at a rate of 0.35 nm/s.

boundaries. The same feature around the same energy level is present in the JC data. Previous theoretical studies modeling the effect of grain boundaries have suggested that they lead to higher loss in a certain wavelength range determined by the average size⁷⁶. These earlier calculations have, in fact, predicted higher loss in this energy range.

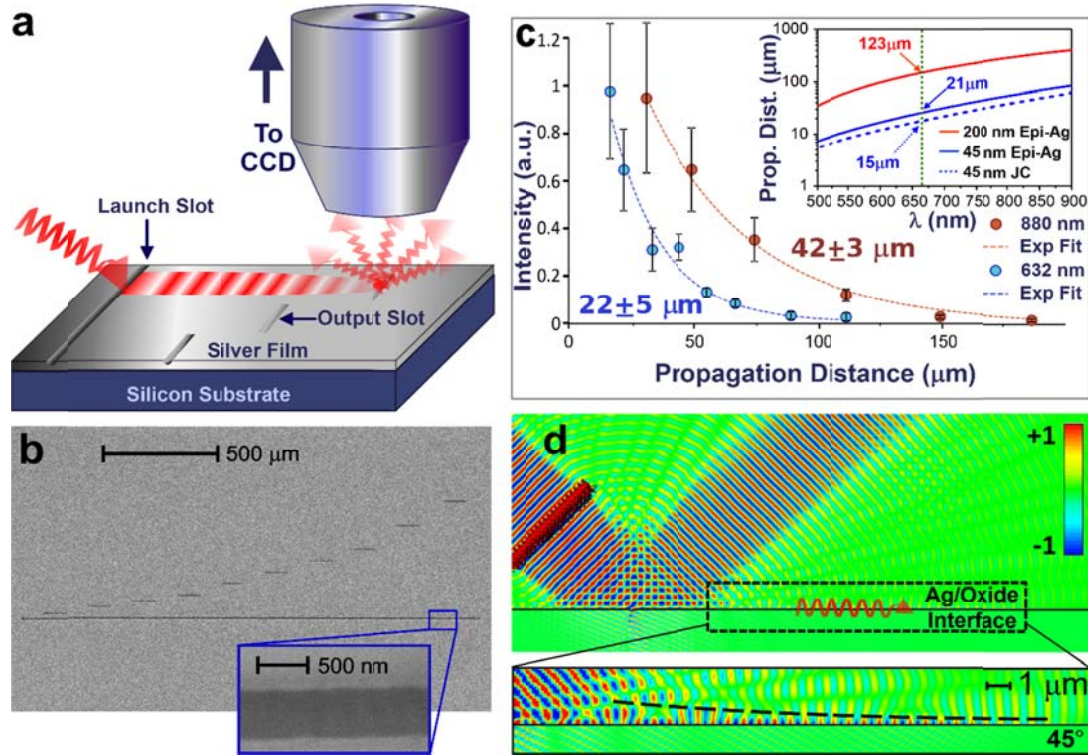


Fig. 12. Schematic, experimental results, and simulations of propagation distance measurements. (a) Schematic of the propagation distance setup. (b) SEM image of the launching and output slots on the 45 nm thick epitaxial Ag film. (c) Propagation measurements for two excitation wavelengths (632 nm and 880 nm). Exponential curves are fitted to the data. The inset, plotted on semilog scale, compares the simulated propagation distances at two different film thicknesses using the measured optical constants. The green dotted line marks the wavelength at 632 nm. (d) Simulation of the mode profile and the SPP excitation at the interface between Ag and the oxide capping layers.

Our measured optical constants suggest improved theoretical limits to the performance of plasmonic devices. In order to experimentally demonstrate these improvements, we measured SPP propagation distances over the 45 nm epitaxial Ag film. We excited and detected the SPPs in reflection geometry, as illustrated in Fig. 12a. Light incident from an oblique angle on a single groove launches the SPPs, which are subsequently detected at a series of output coupling slits with increasing distance from the launching site, as shown in the scanning electron microscope (SEM) image in Fig.

12b. We used two different incident wavelengths (632 nm and 880 nm). The integrated optical signals from the output grooves are plotted as a function of propagation length in Fig. 12c. The experimental data were fitted with simple exponential functions, and we extracted intensity propagation distances of $22 \pm 5 \mu\text{m}$ and $42 \pm 3 \mu\text{m}$ for SPP at 632 nm and 880 nm, respectively. Analytical calculations predict propagation distances of $21 \mu\text{m}$ at 632 nm and $78 \mu\text{m}$ at 880 nm for an ideal layer with the newly extracted permittivity, as shown in the inset of Fig. 12c. The propagation distance measurement at 632 nm is in excellent agreement with the calculated value. It is well known that the SPP propagation distance strongly depends on the film thickness. With a film thickness of 200 nm, for instance, the predicted intensity propagation distance would increase to $123 \mu\text{m}$ at 632 nm and $378 \mu\text{m}$ at 880 nm, respectively. The SPP launching mechanism and expected modal profile is further verified by conducting full-wave simulations of the geometry (Fig. 12d), employing the experimentally retrieved optical parameters.

We suggest that future theoretical calculations on metamaterials and plasmonic devices based on Ag should incorporate the new optical constants reported here, as they better capture the intrinsic properties of bulk Ag. Because we were able to fit the experimental data with a simple, three-component analytical model, these newly extracted optical constants will facilitate the calculation of other important parameters such as the material Q-factor and group velocity in Ag. While the reported optical constants would not apply to low-quality films produced using thermal evaporations, Ag nanoparticles⁷⁷, nanoshell⁷⁸, and nanoplatelets⁷⁹ synthesized using wet chemical procedures are considered to be of single crystalline structure, for which these new optical constant values are expected to apply. We anticipate that these high-quality epitaxial silver films and their improved optical properties will have a significant positive impact on the fields of plasmonics and metamaterials as already demonstrated in the case of nanolasers⁸⁰.

C.6. Progress on the spin wave project

We have mainly three accomplishments in the spin wave project. First, we demonstrated that the spin wave amplitude can be controlled by a direct current in a bilayer structure composed of a heavy metal and a magnetic material via the spin hall effect. Second, we demonstrated the use of the micro-Brillouin light scattering (μ -BLS) technique as a local temperature sensor for magnons in a permalloy (Py) thin film and phonons in the glass substrate. Third, we demonstrate that the spatial decay of spin waves launched by a microwave antenna deviates from an exponential function typically assumed because of interference effects. We focus on the first two accomplishments in this report.

C.6.1. Spin wave amplification

Spin waves are fundamental excitations in magnetic materials. Understanding the excitation, propagation, and damping of spin waves is critical for a wide range of practical applications including magnetic memories, microwave oscillators, and logic devices beyond the conventional CMOS technology. For example, as the data rate in magnetic memory devices reaches gigahertz range, the precessional dynamics associated with spin waves has become relevant in limiting operational speed in these devices. SWs may also serve as a link between phase locked nano-oscillators^{81, 82} or carry spin current in magnetic microstructures subject to a thermal gradient^{83, 84}. SWs have also been proposed for use in an information bus in a hybrid logic device⁸⁵ and for building logic gates⁸⁶.

A major obstacle to many of these applications is the fast damping or short propagation length of SWs in metallic magnetic layers. Current induced magnetization manipulation via spin transfer torque (STT) has been proposed to compensate for the damping of SWs^{87, 88}. The search for efficient STT materials has led to the investigation of metallic bilayer structures consisting of a magnetic layer and a nonmagnetic layer with strong spin-orbit coupling (e.g., Pt⁸⁹⁻⁹², Ta⁹³, and W⁹⁴). In the nonmagnetic layer, spin polarized current is generated via the spin Hall effect (SHE), in which electrons with different spin states are deflected to opposite directions^{95, 96}. Such spin polarized current then exerts a STT on the adjacent magnetic layer, enabling control of magnetization dynamics via electric control.

We investigated the electric control of propagating spin waves (SWs) in a CoBFe/Ta bilayer waveguide as illustrated in Fig. 13. We use μ -BLS to observe the amplitude of the SWs in the bilayer waveguide and its change due to an applied magnetic field and DCs. After removing the effect of heating in the analysis, we observed an 8% change of SW amplitude at a reasonable DC density in a device that has not been fully optimized. Further improvement in device design and fabrication may eventually lead to complete SW damping compensation⁹⁷, thus opening many exciting opportunities in spintronics and magnonics. This accomplishment resulted from collaborations with Prof. Ralph and Prof. Burhman' groups. We reported this result in Physical Review B Rapid communication in 2014.

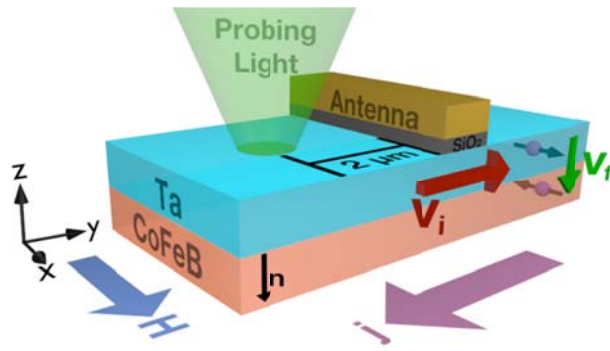


Fig. 13: Schematics of spin polarized current generation in a bilayer and the experimental setup of micro-BLS.

We briefly describe our experimental approach. The μ -BLS technique offers high spatial resolution, sensitivity, and dynamical range as demonstrated in previous experiments⁹⁸⁻¹⁰⁰. The BLS signal arises from the inelastic scattering of light by SWs, and is proportional to the intensity of the SWs, i.e., proportional to the SW amplitude squared. A linearly polarized, single frequency laser beam at 532 nm was focused to a spot size of $\sim 1 \mu\text{m}$ in diameter on the sample. The laser power was approximately 1 mW. The scattered light with orthogonal polarization was collected and sent to a Sandercock multi-pass tandem interferometer to resolve the inelastic scattering from SWs.

For a fixed excitation frequency of 8 GHz and the chosen spatial location (shown in Fig. 13), we scanned the applied magnetic field and DC passing through the bilayer waveguide. We plot the SW amplitude as a function of the applied magnetic field at 10 and -10 mA in Fig. 14(a). There is a clear difference in the SW amplitudes when DCs of opposite sign are applied, which is the key evidence for DC-controlled SW amplification and attenuation. The direction of DC for the SW amplification is consistent with that expected from the SHE, as illustrated in Fig. 13. The value H_R is approximately the magnetic field that corresponds to the peak of the BLS signal in magnetic field dependent spectra (e.g. Fig. 14(a)). As the DC increases, there is a clear shift in H_R as shown in Fig. 14(b), consistent with the heating effect.

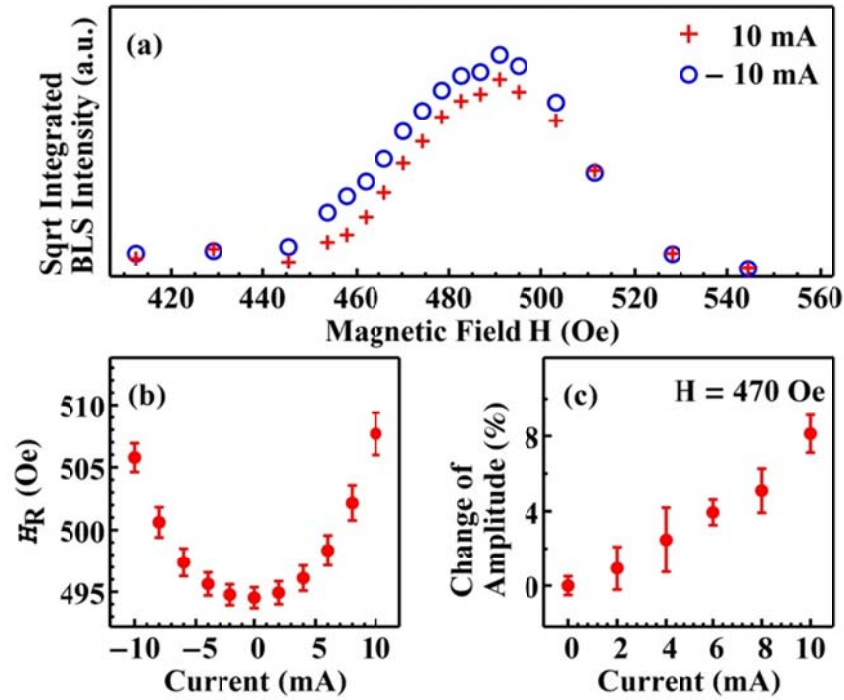


Fig. 14: (a) Magnetic field dependent SW amplitude when DCs of opposite directions were applied. (b) H_R as a function of DCs. (c) Change in the propagating SW amplitude at a particular magnetic field as a function of DCs obtained by subtracting SW amplitudes for DCs of opposite direction.

To isolate the change in the SW amplitude due to the STT arising from the SHE, we remove the effect of heating by comparing the SW amplitudes at two DCs of the same magnitude but opposite directions at a particular magnetic field because the Joule heating should be same for equal magnitude of DCs regardless of their directions. In this context we define $\Delta A = \frac{A_- - A_+}{A_- + A_+}$, where $A_- (A_+)$ corresponds to the SW amplitude for $j < 0$ ($j > 0$). The percentage change in SW amplitude from ΔA at $H = 470$ Oe is plotted in Fig. 14(c). An approximate linear dependence was observed up to the maximal current density applied.

We now estimate the change in damping following the approach outlined in ⁹¹. The spin wave propagating with amplitude $u(x, t)$ can be modeled as $i \frac{\partial u}{\partial t} = \left[\omega_0 + v_g \left(-i \frac{\partial}{\partial x} - k_0 \right) \right] u - i \eta u - i \Delta \eta u$, where ω_0 , k_0 , and v_g are the angular frequency, wave vector, and group velocity, respectively. $\Delta \eta$ represents the STT induced change in the SW decay rate η . In our notation, one has $\Delta \eta < 0$ ($\Delta \eta > 0$) for $j < 0$ ($j > 0$). The SW

amplitude at $x = L$ when a DC is applied can be written as $A_{\mp} = A_0 e^{\pm \frac{|\Delta\eta|L}{v_g}}$, where A_0 is the SW amplitude at 0 mA. When we compare the cases with equal DCs of opposite directions, we obtain $\Delta A = \tanh \frac{|\Delta\eta|L}{v_g}$.

From the data presented in Fig. 14(c), we extracted ΔA at different DCs and calculated $\Delta\eta$ as shown in Fig. 15. In this calculation, we have used $L = 2 \mu\text{m}$ corresponding to the distance from the edge of the antenna to the detection point. The group velocity corresponding to the SW excited at 8 GHz was calculated from the dispersion curve. One can also calculate the change in damping from $\Delta\eta$ using $\Delta\alpha\gamma(H + 2\pi M_{eff}) = \Delta\eta$ (right axis of Fig. 15). If we use an approximate value of $\alpha = 0.008$ from the literature^{93, 101}, the maximal change in damping is about 13% at $I = 10$ mA, corresponding to the current density of 6.3×10^6 A/cm².

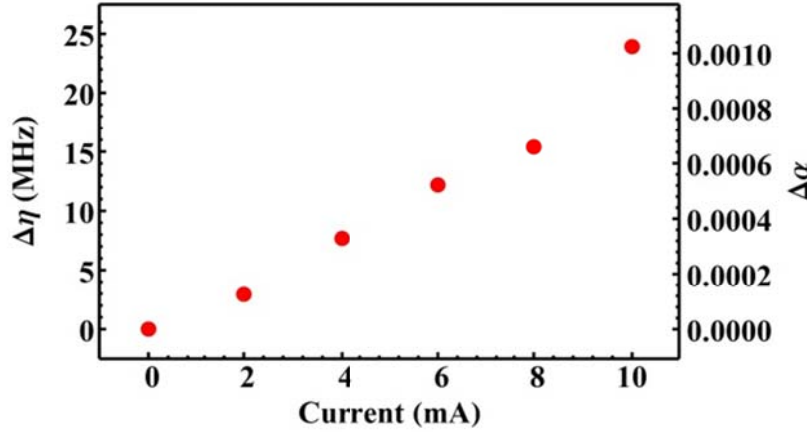


Fig. 15: The change in decay rate (left axis) and damping constant (right axis) as a function of DC.

C.5.2 BLS as a temperature sensor

We demonstrate that the BLS spectra can be used as local temperature sensors for magnons and phonons. Such local temperature sensors may be applied to investigate spin caloritronic and thermal transport phenomena. For example, a key assumption in the current understanding of thermally driven spin currents is that magnons temperature may not reach thermal equilibrium with the phonons locally. This difference between the phonon and magnon temperatures underlies the so called “phonon-magnon drag” that leads to the directional magnon transport or spin current in magnetic insulators and semiconductors¹⁰²⁻¹⁰⁵. Direct experimental confirmation of this phenomenon is currently lacking most likely due to the small temperature difference

between these two temperatures in a sample with a modest temperature gradient¹⁰⁶. This accomplishment resulted from the close collaboration between Prof. Li Shi and is

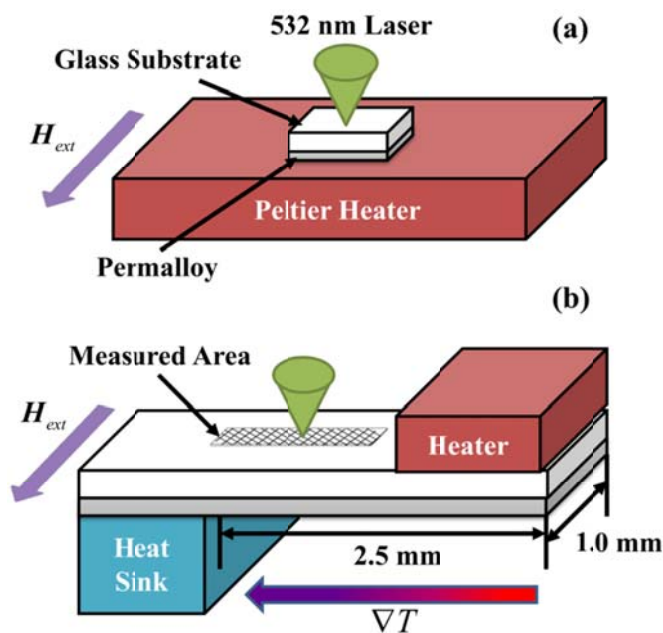


Fig. 16. Experimental schematics. (a) Uniform heating. (b) A thermal gradient is applied laterally to the substrate and perpendicular to the magnetic field.

published in Applied Physics Letters.

Our experimental setup is illustrated in Fig. 16. The sample consists of a Py film sputtered on a glass substrate. The film is nominally 60 nm thick and coated with 10 nm of SiO_x to prevent oxidation. The substrate is a rectangular piece of glass approximately 1 mm wide and 3 mm long. A magnetic field of 500 Oe was applied parallel to the short side of the sample. For the uniform heating measurements (Fig. 17(a)), the sample was mounted on a Peltier heater that was much larger than the sample. For the thermal gradient measurements (Fig. 17(b)), one end of the film was mounted on a resistive heater while the other end was mounted on a heat sink. A thermal gradient was applied along the length of the sample and perpendicular to the external magnetic field.

We first calibrated how the magnon frequencies shift as a function of temperature when the sample is heated uniformly, as shown in Fig. 17. The spectra are dominated by two strong peaks corresponding to the first two perpendicular standing spin wave (PSSW) modes ($n = 1, n = 2$) of the Py film. The PSSW modes are characterized by sinusoidal amplitude profiles in the film thickness direction with the number of nodes corresponding to n . For the relatively small in-plane wave vectors probed in our experiments with normal incident light, the frequencies of the PSSW modes can be

calculated according to,¹⁰ $\omega_n = \gamma \sqrt{(H_{ext} + \frac{2A}{M_S} (\frac{n\pi}{L})^2)(H_{ext} + \frac{2A}{M_S} (\frac{n\pi}{L})^2 + 4\pi M_S)}$, where γ is the gyromagnetic ratio (2.93 MHz/Oe), A (1.0 erg/cm at ~300 K)¹¹ is the exchange constant, H_{ext} is the applied external field, L is the thickness of the ferromagnetic film, and M_S is the saturation magnetization. The temperature dependence of the exchange constant and saturation magnetization cause the mode frequency to vary with temperature.

The magnon frequency was extracted by fitting each PSSW peak in the BLS intensity with a Lorentzian lineshape, as for the magnetic field dependent measurements. The measurements were fit individually and the centers of the peaks were averaged for 24 independent measurements. The error in frequency quoted for each temperature is the standard deviation of the mean. Over the temperature range studied, the frequency decreases linearly with increasing temperature due to the reduced saturation magnetization and exchange constant at higher temperatures. Linear fits to the data yield slopes of $(-8.4 \pm 0.4) \times 10^{-3}$ GHz/K and $(-16.1 \pm 0.8) \times 10^{-3}$ GHz/K for the $n = 1$ and $n = 2$ modes, respectively. The average error in the frequencies for the two modes are 0.02 GHz for $n = 1$ and 0.05 GHz for $n = 2$. Therefore, the measured temperature sensitivities are about 2.4 K and 3.1 K for the $n = 1$ and $n = 2$ modes, respectively. The temperature sensitivities quoted in this study can be further improved simply by extending the measurement time, but the measured values already compare favorably with other nanoscale thermometry techniques¹⁰⁷.

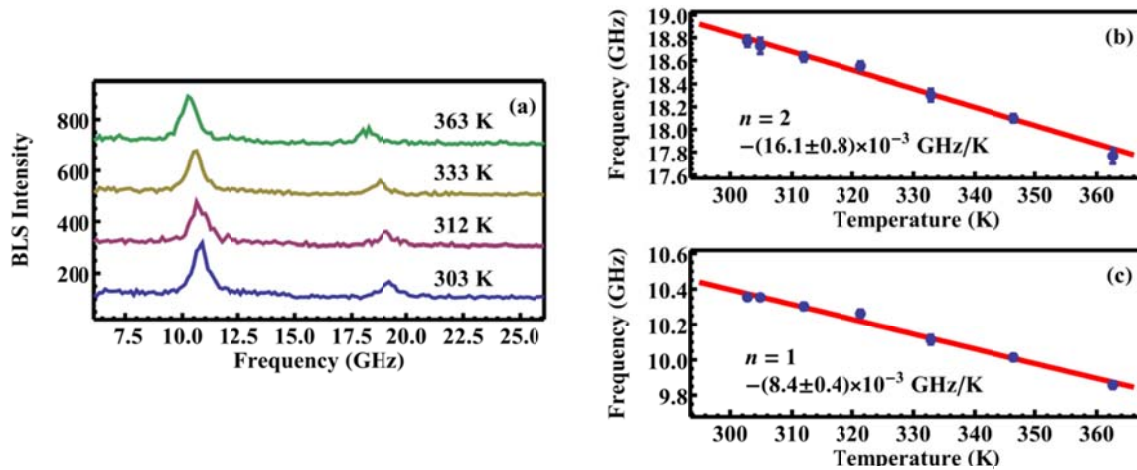


Fig. 17: Temperature dependent thermal magnon spectra in a uniformly heated film. (a) Thermal magnon spectra with increasing temperature from the bottom to the top. Extracted magnon frequencies as a function of temperature for the (b) $n = 1$ and (c) $n = 2$ modes. The solid lines are linear fits, which allow us to determine the frequency shift as a function of temperature.

We now investigate the feasibility of using the BLS spectra as a local magnon temperature sensor. To do so, we establish an in-plane temperature gradient by

mounting the sample to a heater and heat sink, as illustrated in Fig. 17(b). We measure the magnon spectra at different locations along the temperature gradient by moving the sample on a motorized stage in 10 steps of 160 μm each. We performed 24 independent measurements at each position, averaged the peak positions fitted with a Lorentzian lineshape, and quoted the standard deviation of the peak positions as the error bar. To account for the spatial variation of the magnon frequencies due to spatially non-uniform properties of the film, we subtracted the measured magnon frequencies at each location without the thermal gradient from those with the thermal gradient. The resulting magnon frequency shifts for the $n = 2$ and $n = 1$ PSSW modes are displayed in Fig. 18(a) and 18(b), respectively. The spatial dependence of the magnon spectra corresponds to a linear temperature profile, as expected in this simple geometry. We fit

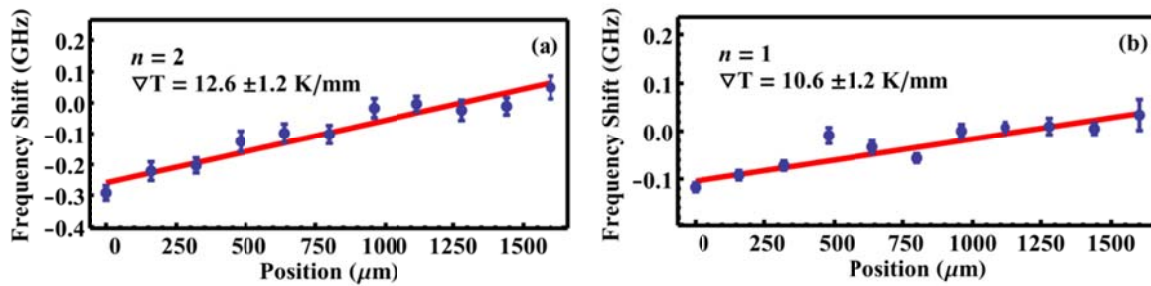


Fig. 18: The extracted magnon frequency shift for the (a) $n = 1$ and (b) $n = 2$ modes as the beam was scanned along the temperature gradient. The magnon frequency without a thermal gradient is subtracted from that with the thermal gradient. The approximate linear shift in magnon frequency is consistent with a linearly varying temperature profile

the frequency shifts to a linear function and obtain shifts of $(-8.9 \pm 1.3) \times 10^{-2} \text{ GHz/mm}$ for the $n = 1$ mode and $(-20 \pm 2) \times 10^{-2} \text{ GHz/mm}$ for the $n = 2$ mode. Using the uniform heating data, the measured frequency shifts correspond to a $-10.6 \pm 1.2 \text{ K/mm}$ temperature gradient between the hot and the cold ends for the $n = 1$ mode and $-12.6 \pm 1.2 \text{ K/mm}$ as measured with the $n = 2$ mode. We note that the temperature gradients extracted from the two PSSW modes are consistent.

To complement the magnon temperature measurement, we measure the acoustic phonon spectra of the glass substrate. The spectrum contains one peak corresponding to the frequency of the acoustic phonons in glass with wave vectors of $4\pi N/\lambda$, where λ is the laser wavelength and N is the index of refraction at the laser wavelength. Assuming $N = 1.5$, the measured frequency of 35 GHz implies a speed of sound of 6 km/s, which is quite reasonable for glass. We first calibrated the change in the phonon spectra as a function of temperature under uniform heating conditions with the setup shown in Fig. 17(a). As the temperature was raised, a systematic increase in the intensity of the phonon peak was observed (Fig. 19(a)), although the peak position did not shift in frequency. Because the ratio between the phonon energy and kT is

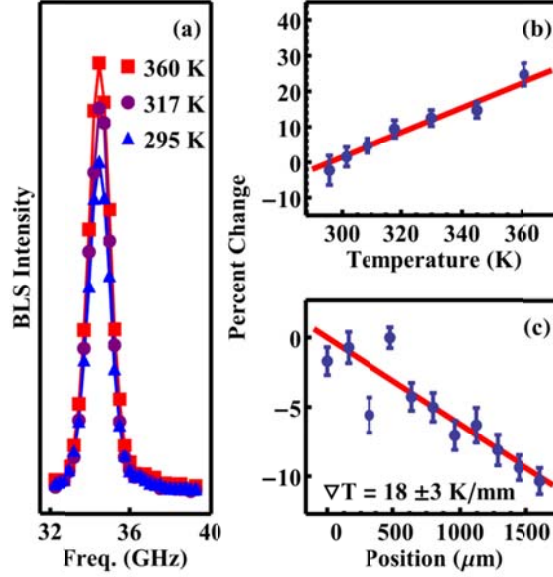


Fig. 19: (a) Phonon spectra of the glass substrate collected at three different temperatures under uniform heating, which shows how the peak intensity increases as the temperature increases. (b) Percent change of the intensity of the phonon peak as the temperature was increased under uniform heating. (c) Percent change of the intensity as the beam was scanned along the temperature gradient, which shows a linearly varying temperature profile.

small, the Bose-Einstein distribution for the phonon mode is reduced to the classical limit that depends linearly on temperature, i.e., $\langle n \rangle = 1/(\exp(\hbar\omega/kT) - 1) \approx kT/\hbar\omega$. Consequently, the intensity of the phonon peak in the BLS spectra depends linearly on temperature, as shown in Fig. 19 (b). The intensities plotted in Fig. 19(b) are the averaged value from 24 measurements with the standard deviation displayed as the error bar. A linear fit yields that the phonon intensity increased by $22 \pm 2 \%$ as the temperature increased from 296 K to 360 K, also an increase of 22 %. The slope of the linear fit is $0.35 \pm 0.03 \text{ \%}/\text{K}$. To measure the local temperature of the sample with a thermal gradient, we subtracted the intensities at each point with and without the thermal gradient to compensate for non-uniformities in the substrate. The data shown in Fig. 19 (c) is fit with a linear function with a slope of $6.3 \pm 1.1 \text{ \%}/\text{mm}$. Using the slope obtained from the uniform heating data, this change in BLS intensity of the phonon mode implies a temperature gradient of $18 \pm 3 \text{ K/mm}$ over the region measured, which is somewhat larger than the value extracted from the magnon spectra but still within two standard deviations. Further work is required to understand whether a difference exists between the phonon and the magnon temperature gradients due to local non-equilibrium between phonons in the glass substrate and magnons in the Py film.

C.6.3 Deviation from exponential decay of spin wave

We investigated the propagation of magnetostatic surface spin waves (MSSW) in a continuous Py thin film excited by an asymmetric coplanar waveguide antenna. The

spin waves were excited in the Damon-Eshbach¹⁰⁸ configuration, wherein a static magnetic field was applied parallel to the antenna and perpendicular to the propagation direction of the spin waves. While mapping the spatial dependence of the surface spin wave intensity, we observed a significant deviation from the simple exponential decay due to damping: an oscillatory signal is superimposed on top of the exponential decay. To model the observed complicated spatial dependent spin wave intensity, we use a closed-form expression that includes contributions from the propagating spin wave and a background magnetization with spatially uniform phase. This simplified closed-form model allows us to fit the experimental data and to extract several key parameters including the wave vectors, the group velocities, and the propagation lengths of the excited spin waves. This result is published in Applied Physics Letters.

D. Conference and Seminar Presentation:

1. Chihhui Wu, Farbod Shafiei, Yanwen Wu, Akshay Singh, **Xiaoqin Li**, Gennady Shvets "A Plasmonic Protractor", CLEO, San Jose, California, June 13th, 2013.
2. Farbod Shafiei, Francesco Monticone, Le Quang Khai, Xing-Xiang Liu, Tom Hartsfield, Andrea Alu, **Xiaoqin Li**, "A subwavelength plasmonic metamolecule exhibiting magnetic based optical Fano resonance", CLEO, San Jose, California, June 12th, 2013.
3. Farbod Shafiei, Francesco Monticone, Le Quang Khai, Xing-Xiang Liu, Tom Hartsfield, Andrea Alu, **Xiaoqin Li**, "A subwavelength plasmonic metamolecule exhibiting magnetic based optical Fano resonance", APS March meeting, March 21st, 2013, Baltimore, MD.
4. Yanwen Wu, Chengdong Zhang, jisun Kim, Matt Zhang, Chih-Kang Shih, **Xiaoqin Li**, "New optical constants of Silver obtained from Atomically Smooth Epitaxial Silver Film", APS March meeting, March 20th, 2013, Baltimore, MD.
5. Daniel R. Birt, Kyongmo An, Maxim Tsoi, Shingo Tamaru, David Ricketts, Kin L Wong, Pedram Khalili Amiri ; Kang L Wang. ; **Xiaoqin Li** "Deviation from Exponential Decay for Spin Waves Excited with an Coplanar Waveguide Antenna", MMM, Chicago, January 15th, 2013.
6. Xiaoqin Li "Lego Approach to Plasmonics" University of Vanderbilt, OSA travelling lecture for student chapters program, September, 25th, 2013
7. Xiaoqin Li. " Imaging and Controlling Spin Waves in Micro-magnetic microstructures", SPIE Photonics, San Diego, California, August 29th, 2013,
8. Xiaoqin Li, "Lego Approach to Plasmonics and Fundamental Optical Properties of Silver", Fundamental Optical Properties of Semiconductors, Kodiak, Alaska, August 16th, 2013
9. Xiaoqin Li, "Light Scattering from Collective Modes of Electrons", Seminar in University of Science and Technology of China, Hefei, China, May 27th, 2013.
10. Xiaoqin Li, "Light Scattering from Collective Modes of Electrons", Seminar in Beijing University. China, May 21th, 2013.
11. Xiaoqin Li, "Light Scattering from Collective Modes of Electrons", Seminar in Beijing Normal University. China, May 24th, 2013.
12. Xiaoqin Li, "Lego Approach to Plasmonics", Seminar in the National NanoScience Center in Beijing China, May 23rd, 2013.

13. Xiaoqin Li, "Lego Approach to Plasmonics", Colloquium in the physics department at the University of Kansas, April 15th, 2013.
14. Xiaoqin Li, "Imaging and Controlling Spin Waves in Magnetic Microstructures" Seminar in the Physics Department at the University of Kansas, April 15, 2013
15. Xiaoqin Li "Fundamental Optical Properties of Silver", Seminar at National Tsing Hua University, Taiwan, December, 16th, 2013
16. Xiaoqin Li "Lego Approach to Plasmonics" University of Texas-Arlington, IEEE Photonics lecture for student chapters program, October, 11th, 2013
17. Xiaoqin Li "Coherent Electronic Coupling in Atomically Thin Semiconductors", NOEKS, September 26th, 2014, Germany.
18. Xiaoqin Li "Coherent Electronic Coupling in Atomically Thin Semiconductors", Seminar at Technical University of Berlin, July 18th, 2014
19. Xiaoqin Li "Plasmonic nanostructures by design", colloquium in the physics department at Dortmund University, July 15th, 2014.
20. Xiaoqin Li "Coherent Electronic Coupling in Atomically Thin Semiconductors", Seminar at Nanjing University, June 18th, 2014
21. Xiaoqin Li "Plasmonic nanostructures by design", seminar at Nanjing University, June 17, 2014.
22. Xiaoqin Li "Two-dimensional View of Electron Dynamics", Invited presentation at the APS March meeting, March, 6th, 2014.
23. Xiaoqin Li "Plasmonic Nanostructures by Design", Invited presentation at the SPIE Photonic West, February, 3rd, 2014.
24. Xiaoqin, Li, "Plasmonic Nanostructures by Design" CINT user workshop organized by Los Alamos National Lab, September 21st, Santa Fe, NM, 2015
25. Xiaoqin Li "Plasmonic Nanostructures by Design" AMOLF, Netherland, July, 2015,
26. Xiaoqin Li "Ultrafast Spectroscopy of Excitons in Atomically Thin Semiconductors" Seminar in Physics Department at Free University of Berlin, May, 2015,
27. Xiaoqin Li "Probing and Controlling Magnons" Seminar in Physics Department at Free University of Berlin, July, 2015,
28. Xiaoqin Li, "Plasmonic Nanostructures by Design", MRS Spring meeting, April 9th, San Francisco, CA, USA.
29. Xiaoqin Li, "Coherent Quantum Dynamics of Excitons in Atomically Thin Semiconductors", MRS Spring meeting, April 7th, San Francisco, CA, USA.
30. Xiaoqin Li, "Light-Matter Interaction on the Nanoscale", National TsingHua University, Materials science and technology department March 26th, 2015
31. Xiaoqin Li, "Light-Matter Interaction on the Nanoscale", INL, Portugal, Jan 28th, 2015.
32. Xiaoqin Li, "Light-Matter Interaction on the Nanoscale", University of Aveiro, Portugal, Jan 27th, 2015
33. Xiaoqin Li "Intrinsic Homogeneous Linewidth and Broadening Mechanisms of Excitons in Atomically Thin Semiconductors"; Physics of Quantum Electronics, Snowbird, Utah, Jan 8th, 2015

Reference

1. Alu, A.; Engheta, N. *Opt. Express* **2009**, 17, (7), 5723-5730.
2. Merlin, R. *Proceedings of the National Academy of Sciences* **2009**, 106, (6), 1693-1698.
3. Shvets, G.; Urzhumov, Y. A. *Phys. Rev. Lett.* **2004**, 93, (24), 243902.
4. Liu, N.; Fu, L.; Kaiser, S.; Schweizer, H.; Giessen, H. *Advanced Materials* **2008**, 20, (20), 3859-3865.
5. Alù, A.; Salandrino, A.; Engheta, N. *Opt. Express* **2006**, 14, (4), 1557-1567.
6. Podolskiy, V.; Sarychev, A.; Shalaev, V. *Opt. Express* **2003**, 11, (7), 735-745.
7. Landau, L. D.; Lifshitz, E. M., *Electrodynamics of continuous media* Pergamon Press ; Addison-Wesley: Oxford : Reading, Mass. :, 1960.
8. Luk'yanchuk, B.; Zheludev, N. I.; Maier, S. A.; Halas, N. J.; Nordlander, P.; Giessen, H.; Chong, C. T. *Nature Materials* **2010**, 9, (9), 707-715.
9. Hao, F.; Sonnefraud, Y.; Dorpe, P. V.; Maier, S. A.; Halas, N. J.; Nordlander, P. *Nano Lett.* **2008**, 8, (11), 3983-3988.
10. Verellen, N.; Sonnefraud, Y.; Sobhani, H.; Hao, F.; Moshchalkov, V. V.; Dorpe, P. V.; Nordlander, P.; Maier, S. A. *Nano Lett.* **2009**, 9, (4), 1663-1667.
11. Francescato, Y.; Giannini, V.; Maier, S. A. *ACS Nano* **2012**, 6, (2), 1830-1838.
12. Brown, L. V.; Sobhani, H.; Lassiter, J. B.; Nordlander, P.; Halas, N. J. *Acs Nano* **2010**, 4, (2), 819-832.
13. Yuan, H.-K.; Chettiar, U. K.; Cai, W.; Kildishev, A. V.; Boltasseva, A.; Drachev, V. P.; Shalaev, V. M. *Opt. Express* **2007**, 15, (3), 1076-1083.
14. Shalaev, V. M. *Nat Photon* **2007**, 1, (1), 41-48.
15. Pendry, J. B. *Physical Review Letters* **2000**, 85, (18), 3966-3969.
16. Prodan, E.; Radloff, C.; Halas, N. J.; Nordlander, P. *Science* **2003**, 302, (5644), 419-422.
17. Moskovits, M. *Rev. Mod. Phys.* **1985**, 57, (3), 783 - 826.
18. Xu, H.; Bjerneld, E. J.; Käll, M.; Börjesson, L. *Physical Review Letters* **1999**, 83, (21), 4357-4360.
19. Kühn, S.; Håkanson, U.; Rogobete, L.; Sandoghdar, V. *Physical Review Letters* **2006**, 97, (1), 017402.
20. Sokolov, K.; Chumanov, G.; Cotton, T. M. *Analytical Chemistry* **1998**, 70, (18), 3898-3905.
21. Anker, J. N.; Hall, W. P.; Lyandres, O.; Shah, N. C.; Zhao, J.; Van Duyne, R. P. *Nature Materials* **2008**, 7, (6), 442-453.
22. Stewart, M. E.; Anderton, C. R.; Thompson, L. B.; Maria, J.; Gray, S. K.; Rogers, J. A.; Nuzzo, R. G. *Chem. Rev.* **2008**, 108, (2), 494-521.
23. Bergman, D. J.; Stockman, M. I. *Phys. Rev. Lett.* **2003**, 90, (2), 027402.
24. Oulton, R. F.; Sorger, V. J.; Zentgraf, T.; Ma, R.-M.; Gladden, C.; Dai, L.; Bartal, G.; Zhang, X. *Nature* **2009**, 461, (7264), 629-632.
25. Noginov, M. A.; Zhu, G.; Belgrave, A. M.; Bakker, R.; Shalaev, V. M.; Narimanov, E. E.; Stout, S.; Herz, E.; Suteewong, T.; Wiesner, U. *Nature* **2009**, 460, (7259), 1110-1112.
26. Miroshnichenko, A. E.; Flach, S.; Kivshar, Y. S. *Rev. Mod. Phys.* **2010**, 82, (3), 2257-2298.
27. Fedotov, V. A.; Rose, M.; Prosvirnin, S. L.; Papasimakis, N.; Zheludev, N. I. *Physical Review Letters* **2007**, 99, (14), 147401.
28. Zhang, S.; Genov, D. A.; Wang, Y.; Liu, M.; Zhang, X. *Physical Review Letters* **2008**, 101, (4), 047401.
29. Verellen, N.; Sonnefraud, Y.; Sobhani, H.; Hao, F.; Moshchalkov, V. V.; Van Dorpe, P.; Nordlander, P.; Maier, S. A. *Nano Letters* **2009**, 9, (4), 1663-1667.
30. Liu, N.; Langguth, L.; Weiss, T.; Kastel, J.; Fleischhauer, M.; Pfau, T.; Giessen, H. *Nat. Mater.* **2009**, 8, (9), 758-762.

31. Mukherjee, S.; Sobhani, H.; Lassiter, J. B.; Bardhan, R.; Nordlander, P.; Halas, N. J. *Nano Lett.* **2010**, 10, (7), 2694-2701.
32. Fan, J. A.; Bao, K.; Wu, C.; Bao, J.; Bardhan, R.; Halas, N. J.; Manoharan, V. N.; Shvets, G.; Nordlander, P.; Capasso, F. *Nano Letters* **2010**, 10, (11), 4680-5.
33. Wu, C. H.; Khanikaev, A. B.; Adato, R.; Arju, N.; Yanik, A. A.; Altug, H.; Shvets, G. *Nat. Mater.* **2012**, 11, (1), 69-75.
34. Sonnichsen, C.; Reinhard, B. M.; Liphardt, J.; Alivisatos, A. P. *Nat Biotechnol* **2005**, 23, (6), 741-745.
35. Jun, Y. W.; Sheikholeslami, S.; Hostetter, D. R.; Tajon, C.; Craik, C. S.; Alivisatos, A. P. *P Natl Acad Sci USA* **2009**, 106, (42), 17735-17740.
36. Liu, N.; Hentschel, M.; Weiss, T.; Alivisatos, A. P.; Giessen, H. *Science* **2011**, 332, (6036), 1407-1410.
37. Schaefer, D. M.; Reifenberger, R.; Patil, A.; Andres, R. P. *Appl. Phys. Lett.* **1995**, 66, (8), 1012-1014.
38. Baur, C.; Bugacov, A.; Koel, B. E.; Madhukar, A.; Montoya, N.; Ramachandran, T. R.; Requicha, A. A. G.; Resch, R.; Will, P. *Nanotech* **1998**, 9, (4), 360-364.
39. Kim, S.; Shafiei, F.; Ratchford, D.; Li, X. Q. *Nanotech* **2011**, 22, (11), 115301.
40. Junno, T.; Deppert, K.; Montelius, L.; Samuelson, L. *Appl. Phys. Lett.* **1995**, 66, (26), 3627-3629.
41. Engheta, N.; Salandrino, A.; Alù, A. *Phys. Rev. Lett.* **2005**, 95, 095504.
42. Engheta, N. *Science* **2007**, 317, 1698-1702.
43. Alù, A.; Engheta, N. *Phys. Rev. Lett.* **2009**, 103, 143902.
44. Sun, Y.; Edwards, B.; Alù, A.; Engheta, N. *Nat. Mater.* **2012**, 11, 208-212.
45. Haus, H. A.; Lai, Y. *J. Light. Technol.* **1992**, 10, 57-62.
46. Haus, H. A.; Lai, Y. *IEEE J. Quantum Electron.* **1992**, 28, 205-213.
47. Khan, M. J.; Manolatos, C.; Villeneuve, P. R.; Haus, H. A.; Joannopoulos, J. D. *IEEE J. Quantum Electron.* **1999**, 35, 1451-1460.
48. Kimble, H. J. *Nature* **2008**, 453, (7198), 1023-1030.
49. Duan, L. M.; Kimble, H. J. *Phys. Rev. Lett.* **2004**, 92, (12), 127902.
50. Ritter, S.; Nolleke, C.; Hahn, C.; Reiserer, A.; Neuzner, A.; Uphoff, M.; Mucke, M.; Figueroa, E.; Bochmann, J.; Rempe, G. *Nature* **2012**, 484, (7393), 195-200.
51. Yoshie, T.; Scherer, A.; Hendrickson, J.; Khitrova, G.; Gibbs, H. M.; Rupper, G.; Ell, C.; Shchekin, O. B.; Deppe, D. G. *Nature* **2004**, 432, (7014), 200-203.
52. Englund, D.; Faraon, A.; Fushman, I.; Stoltz, N.; Petroff, P.; Vuckovic, J. *Nature* **2007**, 450, (7171), 857-861.
53. Temnov, V. V.; Woggon, U. *Phys. Rev. Lett.* **2005**, 95, (24), 243602.
54. Ridolfo, A.; Di Stefano, O.; Fina, N.; Saija, R.; Savasta, S. *Phys. Rev. Lett.* **2010**, 105, (26), 263601.
55. Shimizu, K. T.; Woo, W. K.; Fisher, B. R.; Eisler, H. J.; Bawendi, M. G. *Phys. Rev. Lett.* **2002**, 89, (11), 117401.
56. Anger, P.; Bharadwaj, P.; Novotny, L. *Phys. Rev. Lett.* **2006**, 96, (11), 113002.
57. Altewischer, E.; van Exter, M. P.; Woerdman, J. P. *Nature* **2002**, 418, (6895), 304-306.
58. Akimov, A. V.; Mukherjee, A.; Yu, C. L.; Chang, D. E.; Zibrov, A. S.; Hemmer, P. R.; Park, H.; Lukin, M. D. *Nature* **2007**, 450, (7168), 402-406.
59. Fakonas, J. S.; Lee, H.; Kelaita, Y. A.; Atwater, H. A. *Nat Photon* **2014**, 8, (4), 317-320.
60. Zhang, W.; Govorov, A. O.; Bryant, G. W. *Phys. Rev. Lett.* **2006**, 97, (14), 146804.
61. Chen, X.-W.; Sandoghdar, V.; Agio, M. *Phys. Rev. Lett.* **2013**, 110, (15), 153605.
62. Shafiei, F.; Wu, C.; Wu, Y.; Khanikaev, A. B.; Putzke, P.; Singh, A.; Li, X.; Shvets, G. *Nat Photon* **2013**, 7, (5), 367-372.
63. Junno, T.; Deppert, K.; Montelius, L.; Samuelson, L. *Appl. Phys. Lett.* **1995**, 66, (26), 3627-3629.

64. Kim, S.; Ratchford, D. C.; Li, X. Q. *Acs Nano* **2009**, 3, (10), 2989-2994.
65. Ratchford, D.; Shafiei, F.; Kim, S.; Gray, S. K.; Li, X. Q. *Nano Lett.* **2011**, 11, (3), 1049-1054.
66. Boltasseva, A.; Atwater, H. A. *Science* **2011**, 331, (6015), 290-291.
67. Khurgin, J. B.; Boltasseva, A. *Mrs Bulletin* **2012**, 37, (8), 768-779.
68. Tassin, P.; Koschny, T.; Kafesaki, M.; Soukoulis, C. M. *Nature Photonics* **2012**, 6, (4), 259-264.
69. Huang, L.; Chey, S. J.; Weaver, J. H. *Surface Science* **1998**, 416, (1-2), L1101-L1106.
70. Smith, A. R.; Chao, K. J.; Niu, Q.; Shih, C. K. *Science* **1996**, 273, (5272), 226-228.
71. Hornvonnhoegen, M.; Schmidt, T.; Meyer, G.; Winau, D.; Rieder, K. H. *Physical Review B* **1995**, 52, (15), 10764-10767.
72. Johnson, P. B.; Christy, R. W. *Physical Review B* **1972**, 6, (12), 4370-4379.
73. Arwin, H.; Aspnes, D. E. *Thin Solid Films* **1984**, 113, (2), 101-113.
74. Hilfiker, J. N.; Singh, N.; Tiwald, T.; Convey, D.; Smith, S. M.; Baker, J. H.; Tompkins, H. G. *Thin Solid Films* **2008**, 516, (22), 7979-7989.
75. Pribil, G. K.; Johs, B.; Ianno, N. J. *Thin Solid Films* **2004**, 455, 443-449.
76. Hunderi, O. *Physical Review B* **1973**, 7, (8), 3419-3429.
77. Sun, Y. G.; Xia, Y. N. *Science* **2002**, 298, (5601), 2176-2179.
78. Ben Moshe, A.; Markovich, G. *Chemistry of Materials* **2011**, 23, (5), 1239-1245.
79. Jiang, L. P.; Xu, S.; Zhu, J. M.; Zhang, J. R.; Zhu, J. J.; Chen, H. Y. *Inorganic Chemistry* **2004**, 43, (19), 5877-5883.
80. Lu, Y.-J.; Kim, J.; Chen, H.-Y.; Wu, C.; Dabidian, N.; Sanders, C. E.; Wang, C.-Y.; Lu, M.-Y.; Li, B.-H.; Qiu, X.; Chang, W.-H.; Chen, L.-J.; Shvets, G.; Shih, C.-K.; Gwo, S. *Science* **2012**, 337, (6093), 450-453.
81. Kaka, S.; Pufall, M. R.; Rippard, W. H.; Silva, T. J.; Russek, S. E.; Katine, J. A. *Nature* **2005**, 437, (7057), 389-392.
82. Demidov, V. E.; Urazhdin, S.; Demokritov, S. O. *Nat Mater* **2010**, 9, (12), 984-988.
83. Uchida, K.; Takahashi, S.; Harii, K.; Ieda, J.; Koshibae, W.; Ando, K.; Maekawa, S.; Saitoh, E. *Nature* **2008**, 455, 778-81.
84. Bauer, G. E. W.; Saitoh, E.; van Wees, B. J. *Nat Mater* **2012**, 11, (5), 391-399.
85. Wolf, S. A.; Awschalom, D. D.; Buhrman, R. A.; Daughton, J. M.; von Molnar, S.; Roukes, M. L.; Chtchelkanova, A. Y.; Treger, D. M. *Science* **2001**, 294, (5546), 1488-1495.
86. Schneider, T.; Serga, A. A.; Leven, B.; Hillebrands, B.; Stamps, R. L.; Kostylev, M. P. *Applied Physics Letters* **2008**, 92, (2), 022505-3.
87. Li, Z.; Zhang, S. *Physical Review Letters* **2004**, 92, (20), 207203.
88. Seo, S.-M.; Lee, K.-J.; Yang, H.; Ono, T. *Physical Review Letters* **2009**, 102, 147202.
89. Demidov, V. E.; Urazhdin, S.; Edwards, E. R. J.; Stiles, M. D.; McMichael, R. D.; Demokritov, S. O. *Physical Review Letters* **2011**, 107, (10), 107204.
90. Liu, L.; Moriyama, T.; Ralph, D.; Buhrman, R. *Physical Review Letters* **2011**, 106, 036601.
91. Wang, Z.; Sun, Y.; Wu, M.; Tiberkevich, V.; Slavin, A. *Physical Review Letters* **2011**, 107, (14), 146602.
92. Miron, I. M.; Garello, K.; Gaudin, G.; Zermatten, P.-J.; Costache, M. V.; Auffret, S.; Bandiera, S.; Rodmacq, B.; Schuhl, A.; Gambardella, P. *Nature* **2011**, 476, (7359), 189-193.
93. Liu, L.; Pai, C. F.; Li, Y.; Tseng, H. W.; Ralph, D. C.; Buhrman, R. A. *Science* **2012**, 336, (6081), 555-8.
94. Pai, C.-F.; Liu, L.; Li, Y.; Tseng, H. W.; Ralph, D. C.; Buhrman, R. A. *Applied Physics Letters* **2012**, 101, (12), 122404.
95. Hirsch, J. E. *Physical Review Letters* **1999**, 83, 1834.
96. Dyakonov, M. I.; Perel, V. I. *Physics Letters A* **1971**, 35, (6), 459-460.
97. Suhl, H. *Physical Review* **1955**, 97, (2), 555-557.
98. Demokritov, S. O.; Demidov, V. E. *Magnetics, IEEE Transactions on* **2008**, 44, 6-12.

99. Madami, M.; Bonetti, S.; Consolo, G.; Tacchi, S.; Carlotti, G.; Gubbiotti, G.; Mancoff, F. B.; Yar, M. A.; Akerman, J. *Nat Nano* **2011**, 6, (10), 635-638.
100. Demidov, V. E.; Demokritov, S. O.; Hillebrands, B.; Laufenberg, M.; Freitas, P. P. *Applied Physics Letters* **2004**, 85, (14), 2866-2868.
101. Bilzer, C.; Devolder, T.; Kim, J.-V.; Counil, G.; Chappert, C.; Cardoso, S.; Freitas, P. P. *Journal of Applied Physics* **2006**, 100, (5), 053903-4.
102. Jaworski, C.; Yang, J.; Mack, S.; Awschalom, D.; Myers, R.; Heremans, J. *Physical Review Letters* **2011**, 106, (18), 186601.
103. Sanders, D.; Walton, D. *Physical Review B* **1977**, 15, (3), 1489-1494.
104. Adachi, H.; Uchida, K.-i.; Saitoh, E.; Ohe, J.-i.; Takahashi, S.; Maekawa, S. *Applied Physics Letters* **2010**, 97, (25), 252506.
105. Uchida, K.; Adachi, H.; An, T.; Ota, T.; Toda, M.; Hillebrands, B.; Maekawa, S.; Saitoh, E. *Nat Mater* **2011**, 10, (10), 737-741.
106. Agrawal, M.; Vasyuchka, V.; Serga, A.; Karenowska, A.; Melkov, G.; Hillebrands, B. *Physical Review Letters* **2013**, 111, (10), 107204.
107. Cahill, D. G.; Goodson, K.; Majumdar, A. *Journal of Heat Transfer* **2001**, 124, (2), 223-241.
108. Damon, R. W.; Eshbach, J. R. *Journal of Physics and Chemistry of Solids* **1961**, 19, (3-4), 308-320.

1.

1. Report Type

Final Report

Primary Contact E-mail**Contact email if there is a problem with the report.**

elaineli@physics.utexas.edu

Primary Contact Phone Number**Contact phone number if there is a problem with the report**

512-471-2063

Organization / Institution name

University of Texas-Austin

Grant/Contract Title**The full title of the funded effort.**

Light-Matter Interaction on the Nanoscale

Grant/Contract Number**AFOSR assigned control number. It must begin with "FA9550" or "F49620" or "FA2386".**

FA9550-10-1-0022

Principal Investigator Name**The full name of the principal investigator on the grant or contract.**

Xiaoqin Li

Program Manager**The AFOSR Program Manager currently assigned to the award**

Gernot Pomrenke

Reporting Period Start Date

10/01/2009

Reporting Period End Date

09/30/2015

Abstract

Studies of light-matter interactions in quantum-confined systems and nanostructures have provided great insight into diverse and fundamental problems such as many-body interactions and entanglement. In particular, optical spectroscopy has proved to be a powerful tool for elucidating electronic dynamics owing to its ability to access information that is difficult or impossible to obtain otherwise. The knowledge obtained from optical spectroscopic studies complement those obtained from other techniques and provide a more accurate picture of system dynamics. For example, electronic properties of materials are mainly determined by transitions within one energy band, which describe carrier transport in real space. On the other hand, optical properties are often related to transitions between valence and conduction bands. However, a strict separation between intraband and interband phenomena is impossible since both are simultaneously present and critical for determining the performance limit of future opto-electronic devices needed in DoD operations and future commercial products required by the society striving on modern technologies.

In the initial proposal, we outlined two specific projects: (i) investigation of coherent electronic coupling in semiconductor quantum dot clusters; (ii) investigation of spin wave dynamics in ferromagnetic multilayer structures. In the course of the project, we have expanded the first direction to include investigation of metallic nanoparticles and clusters as well as hybrid nanostructures consisted of both metallic and

DISTRIBUTION A: Distribution approved for public release.

semiconductor components. In addition, we have studied an emerging class of atomically thin semiconductors known as the transition metal dichalcogenides. In this report, we summarize the key progress occurred during the past 6 years. These results have been broadly disseminated via conferences and scientific literatures. We choose a few representative examples to discuss in this technical report.

Distribution Statement

This is block 12 on the SF298 form.

Distribution A - Approved for Public Release

Explanation for Distribution Statement

If this is not approved for public release, please provide a short explanation. E.g., contains proprietary information.

SF298 Form

Please attach your [SF298](#) form. A blank SF298 can be found [here](#). Please do not password protect or secure the PDF. The maximum file size for an SF298 is 50MB.

[UT-Li-FORM-298.pdf](#)

Upload the Report Document. File must be a PDF. Please do not password protect or secure the PDF. The maximum file size for the Report Document is 50MB.

[Li_UT_AFOSR-FinalReport-2015_v4.pdf](#)

Upload a Report Document, if any. The maximum file size for the Report Document is 50MB.

Archival Publications (published) during reporting period:

see report

Changes in research objectives (if any):

Change in AFOSR Program Manager, if any:

Extensions granted or milestones slipped, if any:

AFOSR LRIR Number

LRIR Title

Reporting Period

Laboratory Task Manager

Program Officer

Research Objectives

Technical Summary

Funding Summary by Cost Category (by FY, \$K)

	Starting FY	FY+1	FY+2
Salary			
Equipment/Facilities			
Supplies			
Total			

Report Document

Report Document - Text Analysis

Report Document - Text Analysis

Appendix Documents

2. Thank You

E-mail user

Dec 20, 2015 04:02:58 Success: Email Sent to: elaineli@physics.utexas.edu
DISTRIBUTION A: Distribution approved for public release.